International Journal of Plasticity 75 (2015) 141–169

Contents lists available at ScienceDirect

International Journal of Plasticity

journal homepage: www.elsevier.com/locate/ijplas

An evolving plane stress yield criterion based on crystal plasticity virtual experiments

Jerzy Gawad [a, b, *], Dorel Banabic [d], Albert Van Bael [c], Dan Sorin Comsa [d], Mihai Gologanu [d], Philip Eyckens [c], Paul Van Houtte [c], Dirk Roose [a]

[a] Department of Computer Science, KU Leuven, Celestijnenlaan 200A, 3001 Leuven, Belgium
[b] AGH University of Science and Technology, al. Mickiewicza 30, 30-059 Krakow, Poland
[c] Department of Materials Engineering, KU Leuven, Kasteelpark Arenberg 44 Box 2450, 3001 Leuven, Belgium
[d] CERTETA Research Center, Technical University of Cluj-Napoca, Memorandumului 28, 400114 Cluj Napoca, Romania

ARTICLE INFO

Article history:
Received 22 August 2014
Received in revised form 23 January 2015
Available online 14 March 2015

Keywords:
A. Yield condition
B. Anisotropic material
B. Constitutive behaviour
B. Crystal plasticity
C. Hierarchical multi-scale modelling

ABSTRACT

This paper presents a new hierarchical multi-scale framework that allows taking into account evolution of the plastic anisotropy during sheet forming processes. The evolution of crystallographic texture, which is identified as the main source of the plastic anisotropy, is predicted by the ALAMEL crystal plasticity model. An extension to the phenomenological anisotropic plane-stress yield criterion BBC2008 is proposed, which provides adaptive updates of the local anisotropy in the integration points of the macroscopic finite element model. To this end, the BBC2008 is systematically recalibrated to data provided by the crystal plasticity virtual experiment framework (VEF). An enhanced identification algorithm is proposed. The new algorithm exploits comprehensive material characterization delivered by the VEF.

The deep drawing of cylindrical cups is used as a benchmark case. An industrial-grade aluminium alloy AA6016 is chosen for the test case. The experimental part of the study includes X-ray diffraction measurements of the texture as well as mechanical testing, which comprises uniaxial tensile tests, a bulge test and the deep drawing of cylindrical cups. A noticeable through-thickness gradient in terms of both the texture and the plastic anisotropy is identified in the initial material. This issue is taken into consideration in the study.

Three groups of simulations have been performed, in which (i) the BBC2008 was calibrated by means of the mechanical tests, (ii) the BBC2008 was calibrated by means of the VEF based on the initial texture, but kept constant throughout the simulation, and (iii) the BBC2008 was systematically recalibrated by means of the VEF to reflect the effects of texture evolution. The earing profiles measured in the experimentally drawn cups are compared to the ones predicted by the simulations. It is found that the cup profile predictions by (i) are clearly inferior compared to both (ii) and (iii). However, in the considered process (iii) provides only a moderate improvement over the results of (ii). The explanation of this limited impact of the anisotropy evolution is based on the analysis of the evolved texture and associated plastic anisotropy.

* Corresponding author. Department of Computer Science, KU Leuven, Celestijnenlaan 200A, 3001 Leuven, Belgium. Tel.: +32 16 327658; fax: +32 16 327996.
E-mail address: jerzy.gawad@cs.kuleuven.be (J. Gawad).

http://dx.doi.org/10.1016/j.ijplas.2015.02.011
0749-6419/

1. Introduction

The plastic anisotropy, as well as many other properties of polycrystalline metals, is generally attributed to the microstructure of the material. One of the most prevailing microstructural factors that controls plastic anisotropy is crystallographic texture. There is a broad variety of attempts in literature to take this fact into account in numerical simulations of metal forming processes.

The microstructure can be explicitly dealt with if a physics-based model is employed. Crystal plasticity theories allow one not only to derive macroscopic mechanical response of the polycrystalline material, but they also provide insights on how the microscopic state evolves with an increasing deformation. Several crystal plasticity frameworks have been proposed over the last decades to answer these challenges.

A first approximation, which is attributed to Sachs (1928), is to use an iso-stress assumption for all grains in a representative volume of polycrystal. The Full Constraints (FC) Taylor–Bishop–Hill homogenization scheme, which was originally proposed by Taylor (1938) and later taken up again by Bishop and Hill (1951b), who proposed a different but equivalent solution method, assumes identical deformation throughout all the grains in the considered volume of the material. These authors proposed two different solution methods, which are both based on the Generalized Schmid Law as the constitutive model for a metallic crystal. An approximate but mathematically convenient alternative is the visco-plastic method by Asaro and Needleman (1985).

Unfortunately, the simple homogenization schemes unrealistically neglect interactions between the grains. To address this issue, several more elaborated homogenization schemes have been established. The Visco-Plastic Self-Consistent (VPSC) model, e.g. Molinari et al. (1997), Lebensohn and Tomé (1993), Lebensohn et al. (2007) considers every crystal in the polycrystalline as an ellipsoidal inclusion embedded in an effective medium. Since the medium comprises all the grains in the considered volume, long-range interactions are captured. Another approach is used by 'cluster' models, which assume that the average plastic velocity gradient of the cluster is equal to the macroscopic velocity gradient. The Grain InterAction (GIA) model proposed by Crumbach et al. (2001) and extended by Engler et al. (2005), as well as the RGC model by Tjahjanto et al. (2010), take into account short-range interactions between next-neighbour grains in an aggregate consisting of eight hexahedral grains. The Advanced LAMEL (ALAMEL) was proposed by Van Houtte et al. (2005) as a generalization of the LAMEL (Van Houtte et al., 1999), which both consider interactions in clusters of two grains. Several improvements to the ALAMEL scheme have been recently proposed, for example by Mánik and Holmedal (2013), Zhang et al. (2015), Arul Kumar et al. (2011), Mahesh (2010).

All these frameworks have an important limitation in common: the microstructure is represented in a statistical way, thus a substantially simplified shape of the grains is generally assumed. The Crystal Plasticity Finite Element Method (CPFEM), e.g. (Peirce et al., 1982; Bate, 1999; Roters et al., 2010) takes a step far forward by explicitly treating complex microstructural morphology in a representative volume element. Recently, considerable attention has been attracted by the Crystal Plasticity Fast Fourier Transform (CP-FFT) method (Lebensohn, 2001; Prakash and Lebensohn, 2009; Roters et al., 2012; Lebensohn et al., 2012; Eisenlohr et al., 2013), which promises substantial improvement over the CPFEM in terms of calculation time, while keeping high spatial resolution in order to capture the details of complex microstructures.

The crystal plasticity models mentioned above provide homogenization framework that allows one to derive macroscopic quantities, such as macroscopic stresses, from relevant quantities at the length scale of grains or even finer. Macroscopic forming processes can in essence be simulated by means of a crystal plasticity model implemented directly into an FE code. A clear advantage of the direct coupling is that the crystal plasticity model locally follows the evolution of anisotropy due to the evolving microstructure, including texture and possibly substructure. A recent review by Roters et al. (2010) provides a detailed overview about the incorporation of crystal plasticity models into the FEM. A remarkable part of recent developments in this field has been focused on materials that pose challenges both in modelling and processing, such as hcp alloys, e.g. Segurado et al. (2012), Izadbakhsh et al. (2012), Knezevic et al. (2013), Galán et al. (2014). This kind of multi-scale computations is computationally very intensive. For detailed analyses of complex forming processes, a more robust micro-macro coupling scheme is desirable.

At the other end of the spectrum, the phenomenological models neglect the microstructural effects and focus on macroscopic mechanical response of the material. The phenomenological yield criteria consider the polycrystalline material as homogeneous at the macroscopic level, and the yield surface depends merely on the macroscopic stress, strain rate, certain strain measures as well as their rates. The microstructural features of the material, such as crystallographic texture, can be indirectly taken into account by means of extensive parametrization of these models. Numerous successful efforts have been made in the last decades to improve the macroscopic anisotropy models, for example Hill (1948), Hosford (1979), Barlat et al. (1991, 1997a,b, 2003b, 2005, 2007), Banabic et al. (2000), Aretz and Barlat (2012, 2013), Banabic et al. (2003, 2005), Comsa and Banabic (2008), Banabic et al. (2010), Yoon et al. (2004, 2006, 2010, 2014), Yoshida et al. (2013), Cazacu et al. (2006), Cazacu and Barlat (2004), Plunkett et al. (2006, 2008), Soare et al. (2008), Soare and Barlat (2010), Van Houtte and Van Bael (2004), Van Houtte et al. (2009), Vegter et al. (2003), Vegter and van den Boogaard (2006). The phenomenological yield loci are generally limited to the initial anisotropy of the material, since it is hardly possible to accurately predict the evolution of the yield surface without taking into account how the microstructure develops during the deformation. Usually it is assumed that the changes to the initial yield locus are negligible. The assumption is approximately valid if the plastic strains are not too large, which admittedly holds in some sheet metal forming processes. Nonetheless, when used in a combination with flow theories, such as the normality flow theory, the phenomenological yield loci provide an efficient technique for capturing the

effects of material anisotropy during the simulation of deformation processes. This approach is nowadays commonly followed in commercial Finite Element (FE) packages dedicated for simulations of metal forming operations.

The assumption on constant anisotropy and, to put it in a broader context, a limited description of the microstructural state are particularly restricting if the deformation involves a considerable strain path change. This issue has been recently addressed by Barlat et al. (2011, 2013, 2014), who proposed the homogeneous yield function-based anisotropic hardening (HAH). The HAH introduces a tensor state variable, called the microstructure deviator, which evolves during plastic deformation. Yet again, this elegant mathematical framework relies on phenomenological evolution equations, although one of components of the microstructure deviator can be considered as associated to crystallographic texture, while another, which evolves rapidly during deformation, can be seen as reflecting material dislocation structure (He et al., 2013).

An extensive body of literature exists on the calibration of phenomenological yield loci by means of mechanical testing. To give only a few examples, Kuwabara et al. (2002), Kuwabara (2007), Vegter et al. (2003), Kuwabara and Sugawara (2013), Yin et al. (2014) use sophisticated experimental setups to measure certain sections of yield loci. Even though certain experiments, such as biaxial tension or biaxial tension-compression tests, can in principle be carried out, in practice there are several limitations that may prevent one from obtaining more thorough characterization of plastic properties. Let these few examples suffice to show common impediments: availability of the experimental facilities, calibration of the equipment to ensure consistency of the results across various types of devices used in the experiments, and, last but not least, economical reasons that may enforce constraints on the experiments (Aretz et al., 2007).

One can also find several examples that combine the strength of the two approaches mentioned above. Some of the crystal plasticity frameworks, most remarkably FC Taylor, VPSC, ALAMEL and CPFEM, have been employed to calibrate phenomenological yield loci, e.g. Savoie and MacEwen (1996), Grytten et al. (2008), Van Houtte et al. (2009), Barlat et al. (2005), Inal et al. (2010), Plunkett et al. (2006), Kim et al. (2007, 2008), Kraska et al. (2009), An et al. (2011), Saai et al. (2013), Yoon et al. (2014). The hierarchical multi-scale approach was followed, in which the fine-scale model provides data needed for identification of the macroscopic one that is based on a different mathematical framework. Generally, the crystal plasticity models have to be evaluated for a huge number of possible stress or strain rate modes, sometimes exceeding one million realizations. This inspired works that aim at decreasing the computational effort related to virtual experiments. For instance, Rousselier et al. (2009) proposed a Reduced Texture Methodology, which does not aim at a complete representation of the real material texture, nor at an accurate modelling of its evolution, but it attempts to improve computational performance of virtual experimentation. It has to be emphasized that the majority of the aforementioned efforts focus on calibrating the initial yield locus, leaving the evolution of the plastic anisotropy unaddressed.

A possible way to capture the influence of microstructural changes on the anisotropic response is to use the crystal plasticity model to calculate some quantities of interest in advance and approximate these in the macroscopic simulation. This can be done by sampling followed by calculating a response surface, for instance by means of multivariate Kriging, as reported by Barton et al. (2008), Knap et al. (2008), Rouet-Leduc et al. (2014). However, the sampling is very expensive if it has to cover the evolution of the microstructural state variables in a multi-dimensional space. Alternatively, a sequence of explicit algebraic yield criteria can be pre-calculated for a finite set of strain levels and interpolated during the macroscopic simulation (Plunkett et al., 2006; Nixon et al., 2010a,b; Knezevic et al., 2013). Nevertheless, it appears problematic that the local state evolution may lead outside the validity range of the interpolation.

A viable method to tackle this problem is to use an adaptive hierarchical multi-scale approach. This can be expediently done by systematic updating the material state, such as texture, by applying local macroscopic deformation rates and subsequent recalibration of the phenomenological plasticity model. Each Gauss integration point of a macroscopic FE mesh can be linked with an evolving yield locus description, as it was successfully demonstrated by Gawad et al. (2013, 2010), Van Bael et al. (2010), Van Houtte et al. (2011) on the Facet plastic potential (Van Houtte et al., 2009), and recently by He et al. (2014) that used the CPB06ex2 yield criterion (Cazacu et al., 2006). The evolution of the plastic anisotropy is therefore taken into account, as well as the evolution of the material state.

In order to be adopted by the sheet forming industry, this last option must provide a clear benefit in terms of improved and more complete predictions, especially for those forming simulations where the modelling error is mainly due to limitations of the material model and not to other factors (such as friction model, process details, etc.). Furthermore, it is expected that a clear advantage is gained in terms of the calculation time:

$$\frac{\text{calculation time of the hierarchical model}}{\text{calculation time of the embedded model}} \ll 1$$

For the completeness of the overview, we mention a few attempts to develop macroscopic constitutive models that would allow deriving the current plastic anisotropy directly from instantaneous crystallographic texture or from constituents of crystal plasticity frameworks, e.g. by Arminjon and Bacroix (1991), Kowalczyk and Gambin (2004), Tsotsova and Böhlke (2009).

In this paper we present a new evolving plane stress yield criterion based on crystal plasticity virtual experiments. The yield criterion is able to capture anisotropy evolution associated with changes to the crystallographic texture during the deformation. The paper is organized as follows: Section 2.1 presents the virtual experimentation framework that provides crystal plasticity data needed for identification of the yield criterion. In Section 2.2 we discuss extensions to the BBC2008 plane stress yield criterion (Comsa and Banabic, 2008), which permit it to adaptively accommodate to changes in the texture.

The results are presented in Section 3. We first discuss the initial characterization of the test material. In the subsequent part we elaborate on the impact of the anisotropy evolution on the macroscopic prediction in a deep drawing of cylindrical cups. Finally, we discuss to what extent this correlates with the changes in the material texture due to the plastic deformation.

2. Hierarchical multi-scale framework for evolving plastic anisotropy

The model presented in this work adapts the notion of hierarchical modelling. Accordingly, the interacting models of different length scales exchange information: *upscaling* defines the flow of information from the finer-scale to the coarser-scale, while the flow in the opposite direction is called *downscaling*. The crucial assumption in the presented approach is that the upscaling and downscaling may involve yet another intermediate model acting as a proxy. On one hand, the proxy provides an expedient approximation of certain quantities that can be predicted by the finer-scale model. On the other hand, the proxy may define criteria that decide whether and when the downscaling should be carried out to update the state of the finer-scale model. Thus, the scheme introduces a certain level of indirection in the interactions between the models operating at different length scales. Obviously, the state variables of the coarser- and finer−scale models are treated separately and non-concurrently. The details of the Hierarchical Multi-Scale (HMS) model of the evolving plastic anisotropy are presented in Gawad et al. (2013). Briefly, the hierarchical framework consists of three layers:

1. macroscopic Finite Element (FE) model, which can be extended by user-defined materials,
2. phenomenological description of material plasticity approximating a micro-mechanical crystal plasticity model, and
3. the crystal plasticity model, which predicts strain evolution of crystallographic texture and associated anisotropy.

In this paper we skip discussion on the first component and focus on the remaining two. Firstly, we will elaborate on the crystal plasticity framework that delivers essential data for recalibration of the phenomenological plasticity model. The phenomenological yield locus and its identification algorithms will be presented next. The HMS model by Gawad et al. (2013) originally used the Facet method, which is a general three-dimensional dual plastic potential (Van Houtte et al., 2009). In this work we explore a less complicated description of the macroscopic yield locus, namely the BBC2008 plane stress yield criterion proposed by Comsa and Banabic (2008). The combined model will be referred to as HMS-BBC2008.

The macroscopic material state variables, such as the stress and strain quantities, as well as the yield locus model and the texture, are expressed in a corotational material reference frame. The reference frame is the defined by directions $\mathbf{e}_1$, $\mathbf{e}_2$, $\mathbf{e}_3$, initially coinciding with the rolling, transverse and normal directions of the sheet.

In the discussed approach a macroscopic isotropic hardening law is used to expand the yield locus. While in principle the hardening behaviour can be derived from the crystal plasticity model, the assumption on the isotropic hardening greatly simplifies the phenomenological description of material plasticity. The plastic anisotropy is then directly attributed to the shape of the yield locus, since no further distortion is introduced by the hardening model.

2.1. Virtual experimentation framework

The crystal plasticity theory considers deformation of individual crystals and deformation of aggregates consisting of many crystals.[1] Although the current work makes use of one of crystal plasticity models, its detailed description is beyond the scope of this paper. The reader is referred to the paper by Van Houtte et al. (2005), which provides a comprehensive discussion of the statistical Taylor-type crystal plasticity theories relevant to this work. This subsection briefly summarizes basic concepts of the rate-independent ALAMEL model proposed by Van Houtte et al. (2005). Since the remaining part of the work concentrates mostly on mechanical aspects, such as yielding, the discussion of texture evolution is omitted for brevity. Whereas the ALAMEL model belongs to the group of "strain-rate-driven" CP models, the latter part of the section addresses the cases where the stress state is more opportune as boundary condition. The two formulations, both built on top of the ALAMEL model, are jointly referred to as the Virtual Experimentation Framework (VEF), which can handle arbitrary stress or strain rate mode.

The crystal plasticity models presented in this section consider an aggregate of grains. Each grain is characterized by its orientation assigned from the Orientation Distribution Function (ODF) $f(g)$. The whole aggregate of grains thus corresponds to a discrete form of the ODF $f_d(g)$.

2.1.1. Single crystal plasticity

Let us consider a single-phase polycrystalline aggregate, consisting of a number of grains. In the Taylor-type models, it is supposed that each grain has homogeneous properties, such as crystal orientation, as well as homogeneous stress and strain distributions over the volume. If a single grain is considered, a local constitutive law has to establish relations between the local stress, strain and rigid body rotation inside the volume of the grain. A crystal plasticity theory, for instance the Generalized Schmidt Law, allows one to account for internal processes, such as slip on various slip systems and the rotation of the crystal lattice, which occur as a response to the external stimuli.

[1] The terms 'grain' and 'crystal' are used interchangeably in this section.

Suppose the local velocity gradient $\mathbf{l}$ is imposed on a single grain. Additive decomposition of the velocity gradient tensor leads to

$$\mathbf{l} = \mathbf{d} + \mathbf{w} \tag{1}$$

where the symmetric part $\mathbf{d}$ is referred to as the local strain rate, and the anti-symmetric part $\mathbf{w}$ is called the local spin. Provided that elasticity is neglected, the strain rate needs to be accommodated through plastic deformation, which is carried by dislocation slip on a number of slip systems and/or by twinning on twinning systems. The further discussion is confined to the plastic slip as the only mechanism of plastic deformation.

The slip systems are defined by the family of symmetrically equivalent slip planes and associated family of slip directions. In fcc materials there are 12 slip systems given by $\{111\}\langle 110\rangle$. The definition of a slip system (s) includes the unit vector $\mathbf{m}^{(s)}$, which is normal to a slip plane that allows shear deformation realized by a dislocation glide. The kinematical equation that relates $\mathbf{l}$ with the slip rates $\dot{\gamma}^{(s)}$ of all active slip systems reads

$$\mathbf{d} = \sum_{s=1}^{N} \mathbf{M}^{(s)} \dot{\gamma}^{(s)} \tag{2}$$

where the Schmidt tensor $\mathbf{M}^{(s)}$ relates the normal to the slip plane with the normalized shear direction $\mathbf{b}^{(s)}$ in which the slip occurs:

$$\mathbf{M}^{(s)} = \frac{1}{2}\left(\mathbf{b}^{(s)} \otimes \mathbf{m}^{(s)} + \mathbf{m}^{(s)} \otimes \mathbf{b}^{(s)}\right) \tag{3}$$

The slip systems that satisfy $\dot{\gamma}^{(s)} \neq 0$ are referred to as the active slip systems. The unknown slip rates can be determined under the energetic assumption, which postulates that minimal plastic work is dissipated per unit time:

$$\dot{W} = \sum_{s=1}^{N} \tau_c^{(s)} \left|\dot{\gamma}^{(s)}\right| \rightarrow \min \tag{4}$$

where τ_c^s is the critical resolved shear stress (CRSS) of the slip system (s). Although the CRSS can in principle be expressed as a function of the accumulated shear in the slip system, in the present paper the hardening of the slip systems is neglected. Furthermore, all the slip systems are supposed to have identical CRSS. This does not undermine generality of the presented approach, since these assumptions can be easily lifted. Moreover, one may argue that for certain classes of materials, such as fcc, the texture evolution and induced plastic anisotropy remain practically insensitive to the microscopic hardening model. Of course, this does not generally hold for all types of materials. Additionally, even a very simple microscopic hardening law may be beneficial in handling complex hardening phenomena (e.g. differential hardening effect), as it was recently demonstrated by Eyckens et al. (2015).

Unfortunately, many combinations of slip systems may possibly satisfy (2) and (4) simultaneously, which is called Taylor ambiguity. To determine which slip systems are actually activated, an additional criterion is generally needed. The interested reader is referred to a recent review by Mánik and Holmedal (2014) for a comprehensive study of various means to solve the Taylor ambiguity. One of possible solutions to the issue is to consider a cluster of grains that impose constraints on each other (Van Houtte et al., 2005).

Once the slip rates are known, the deviatoric stress tensor $\mathbf{s}$ can be calculated, either directly by using the Bishop–Hill theory (Bishop and Hill, 1951a), or by using the minimization method (4) and considering it as the work-conjugate to the imposed strain rate:

$$\dot{W} = \mathbf{s} : \mathbf{d} \tag{5}$$

It also follows that texture evolution can be then predicted as well. The lattice spin $\mathbf{w}^L$, which causes texture evolution, can be found from

$$\mathbf{w} = \mathbf{w}^L + \sum_{s=1}^{N} \mathbf{M}_A^{(s)} \dot{\gamma}^s \tag{6}$$

given the anti-symmetric part of the velocity gradient tensor (1) and the slip rates. $\mathbf{M}_A^{(s)}$ is the anti-symmetric complement to the Schmidt tensor:

$$\mathbf{M}_A^{(s)} = \mathbf{b}^{(s)} \otimes \mathbf{m}^{(s)} - \mathbf{M}^{(s)} = \frac{1}{2}\left(\mathbf{b}^{(s)} \otimes \mathbf{m}^{(s)} - \mathbf{m}^{(s)} \otimes \mathbf{b}^{(s)}\right) \tag{7}$$

2.1.2. Polycrystal plasticity: ALAMEL homogenization

A macroscopic deformation may be imposed onto an aggregate of crystals by specifying the velocity gradient $\mathbf{L}$. This velocity gradient tensor can be additively decomposed into a symmetric part $\mathbf{D}$ and anti-symmetric part $\mathbf{W}$:

$$\mathbf{L} = \mathbf{D} + \mathbf{W} \tag{8}$$

The ALAMEL homogenization scheme postulates that clusters of two grains have to be treated jointly. The two grains are assumed to be neighbours, i.e. they are separated by a grain boundary. The boundary is characterized by its orientation, which at the same time defines a local orthogonal reference frame. By convention, the 3rd axis of the grain boundary reference frame is parallel to the grain boundary normal. The scheme allows relaxations of the macroscopic velocity gradient with respect to simple shear along the boundary between the grains:

$$\mathbf{l}^{(grain_1)} = \mathbf{L} + \sum_{j=1}^{2} \mathbf{K}_{RLX}^{(j)} \dot{\gamma}_{RLX}^{(j)} \tag{9}$$

$$\mathbf{l}^{(grain_2)} = \mathbf{L} - \sum_{j=1}^{2} \mathbf{K}_{RLX}^{(j)} \dot{\gamma}_{RLX}^{(j)} \tag{10}$$

As can be seen, the relaxations in both grains are equal with respect to the magnitude, but oriented in opposite directions. The relaxation slip rates $\dot{\gamma}_{RLX}^{(j)}$ conceptually operate on pseudo slip systems which are shared by the two grains, whereas the slip rates and local spin rates of the clustered grains are different. The relaxation matrices in the grain boundary reference frame are defined as:

$$\mathbf{K}_{RLX}^{(1)} = \begin{bmatrix} 0 & 1 & 0 \\ 0 & 0 & 0 \\ 0 & 0 & 0 \end{bmatrix} \quad \mathbf{K}_{RLX}^{(2)} = \begin{bmatrix} 0 & 0 & 0 \\ 0 & 0 & 1 \\ 0 & 0 & 0 \end{bmatrix} \tag{11}$$

Assuming that the two grains have to simultaneously satisfy the energetic assumption, Equation (4) has to be reformulated as:

$$\dot{W} = \sum_{i=1}^{2} \sum_{s=1}^{N} \left\{ \tau_c^{(i,s)} \left| \dot{\gamma}^{(i,s)} \right| \right\} + \sum_{j}^{2} \tau_r^{(j)} \dot{\gamma}_{RLX}^{(j)} \rightarrow \min \tag{12}$$

where the index i refers to the grains in the pair. Van Houtte et al. (2005) suggests to neglect the pseudo-slip term, although some artificial resistance of the pseudo-slip systems can, in principle, be introduced by letting $\tau_r^{(j)} \neq 0$.

The homogenized stress in the polycrystal is considered as the volume average of contributions from all the grains in the polycrystalline. Let V_i denote the volume of the i-th grain. Provided that the stresses in the individual crystals are expressed in the sample reference frame, the Cauchy stress is calculated as follows:

$$\boldsymbol{S}_H = \left(\sum_{i=1}^{n} V_i \right)^{-1} \sum_{i=1}^{n} V_i \boldsymbol{s}_i \tag{13}$$

2.1.3. Stress driven virtual experiments

As it was discussed in the previous paragraphs, the ALAMEL model requires macroscopic velocity gradient or strain rate as input. However, in many deformation processes it is the stress state that is either known or assumed by certain idealization. In such case the crystal plasticity model would need to predict what macroscopic deformation might be reached under a superimposed macroscopic stress $\boldsymbol{\sigma}$. It is clear from (4)–(5) that the stress state of individual grains in the polycrystalline may deviate from the imposed stress, yet the homogenized stress over the aggregate can still satisfy

$$||\mathbf{S}_H - \mathbf{S}|| < \delta \tag{14}$$

where δ is a sufficiently small number. A stronger requirement (i.e. $||\mathbf{S}_H - \mathbf{S}|| = 0$) might be difficult to satisfy given the fact that only a finite number of crystals is used in the discretized texture.

It can be argued that (14) introduces long range interactions in the model, since certain conditions has to be met over the whole polycrystal. Yet it needs to be emphasized that no Sachs-type iso-stress assumption is made concerning the aggregate.

In this section we present an iterative procedure that allows one to analyse deformation paths defined by macroscopic stress modes, even though a strain-rate driven crystal plasticity model is used. Again, it has to be remarked that the homogenization scheme does not require imposing stress boundary condition on every individual grain, and therefore it is not necessarily satisfied on the grain level. On the grain level Equations (8)–(12) still hold and the microscopic boundary conditions are defined in terms of the velocity gradient. The crystal plasticity model is then considered as a black-box implementing a purely plastic rate-insensitive material. It must allow evaluating the homogenized macroscopic stress $\mathbf{S}_H$ as a response to the macroscopic plastic strain rate $\mathbf{D}$, while keeping the state variables unmodified. An update of the state variables can be independently requested from the black-box.

Since the underlying crystal plasticity model neglects the elastic components of stress and strain rate, the homogenized stress is inherently deviatoric and the corresponding macroscopic strain rate has to satisfy the volumetric incompressibility

condition. Therefore, any of these tensor quantities contains only five independent components, which can be utilized by converting the second-order tensor quantities of deviatoric nature into five-dimensional vectors. Throughout the remaining part of the paper the convention will be used that $\widehat{\mathbf{x}}$ denotes vector representation of rank-two tensor $\mathbf{x}$. Detailed description of the transformation is provided in Appendix A. The primary reason for preferring the five-dimensional vector representation is that the conversion allows one to reduce the dimensionality of the search space, since the constraint $\mathrm{tr}\,\mathbf{x} = 0$ is automatically satisfied by the five-dimensional vector representation.

The fundamental part of the algorithm is to find the macroscopic plastic strain rate mode $\widehat{\mathbf{A}}^*$ that corresponds to the imposed deviatoric stress mode $\widehat{\mathbf{U}}^*$, where

$$\widehat{\mathbf{U}} = \frac{\widehat{\mathbf{S}}}{\left\|\widehat{\mathbf{S}}\right\|} \tag{15}$$

and $\widehat{\mathbf{S}}$ is a five-dimensional vector representing the deviatoric part of the stress tensor $\boldsymbol{\sigma}$ that defines the requested deformation path:

$$\mathbf{S} = \boldsymbol{\sigma} - \frac{\mathrm{tr}\boldsymbol{\sigma}}{3}\mathbf{I} \tag{16}$$

where $\mathbf{I}$ is the identity tensor. This is achieved by solving an unconstrained optimization problem, in which the square norm of the vector-valued residual function

$$\mathbf{f}\left(\widehat{\mathbf{A}}, \widehat{\mathbf{U}}^*\right) = \widehat{\mathbf{U}}^* - \frac{\widehat{\mathbf{S}}_H\left(\widehat{\mathbf{A}}\right)}{\left\|\widehat{\mathbf{S}}_H\left(\widehat{\mathbf{A}}\right)\right\|} \tag{17}$$

is minimized. In the subsequent derivations a simplified notation will be used: $\mathbf{f}(\widehat{\mathbf{A}}, \widehat{\mathbf{U}}^*) = \mathbf{f}(\widehat{\mathbf{A}})$, since the imposed stress mode is considered a constant. The evaluation of the residual function involves a call to the underlying crystal plasticity to calculate the homogenized stress $\mathbf{s}_H$. The search starts from an initial guess $\widehat{\mathbf{A}}_0$, typically chosen as $\widehat{\mathbf{A}}_0 = \widehat{\mathbf{U}}^*$, which corresponds to the property of an isotropic von Mises plastic material. From a current point $\widehat{\mathbf{A}}_{\mathrm{old}}$, the algorithm iteratively uses the trust-region minimization approach (Conn et al., 2000)

$$\min_{\widehat{\mathbf{A}}\in\mathbb{R}^5}\left\|\mathbf{f}\left(\widehat{\mathbf{A}}_{\mathrm{old}}\right) + \mathbf{J}\left(\widehat{\mathbf{A}}_{\mathrm{old}}\right)\left(\widehat{\mathbf{A}}_{\mathrm{new}} - \widehat{\mathbf{A}}_{\mathrm{new}}\right)\right\| \quad \text{subject to} \quad \left\|\widehat{\mathbf{A}}_{\mathrm{new}} - \widehat{\mathbf{A}}_{\mathrm{old}}\right\| \le \delta \tag{18}$$

to find a new guess $\widehat{\mathbf{A}}_{\mathrm{new}} = \widehat{\mathbf{A}}_{\mathrm{old}} + \Delta\widehat{\mathbf{A}}$ that satisfies

$$\min_{\widehat{\mathbf{A}}\in\mathbb{R}^5}\left\|\mathbf{J}^T\left(\widehat{\mathbf{A}}\right)\mathbf{J}\left(\widehat{\mathbf{A}}\right)\Delta\widehat{\mathbf{A}} + \mathbf{J}\left(\widehat{\mathbf{A}}\right)\mathbf{f}\left(\widehat{\mathbf{A}}\right)\right\| \tag{19}$$

where $\Delta\widehat{\mathbf{A}}$ is the trial step, δ is the size of the trial step and J is the Jacobian matrix of the function $\mathbf{f}$. The search is terminated when any of the following criteria is fulfilled: (i) $\left\|\mathbf{f}(\widehat{\mathbf{A}}_{\mathrm{new}})\right\|$ is smaller than a pre-defined threshold f_{tol}, or (ii) $\left\|\Delta\widehat{\mathbf{A}}\right\|$ is smaller than a pre-defined minimal step size, or (iii) the number of iterations exceeds its maximal value.

As can be seen from Equations (18) and (19), the Jacobian matrix has to be calculated often. Since it is not available in a closed form, it has to be computed numerically by a finite difference scheme, which is associated with a considerable cost. However, if the initial guess $\widehat{\mathbf{A}}_0$ is sufficiently close to the solution, one may attempt to locate the minimum under the auxiliary assumption that $\mathbf{J}(\widehat{\mathbf{A}}) = \mathbf{J}(\widehat{\mathbf{A}}_0) = const$. From this assumption it follows that the linearized problem is solved, so (18)–(19) become:

$$\min_{\widehat{\mathbf{A}}\in\mathbb{R}^5}\left\|\mathbf{f}\left(\widehat{\mathbf{A}}_{\mathrm{old}}\right) + \mathbf{J}\left(\widehat{\mathbf{A}}_0\right)\left(\widehat{\mathbf{A}}_{\mathrm{new}} - \widehat{\mathbf{A}}_{\mathrm{new}}\right)\right\| \quad \text{subject to} \quad \left\|\widehat{\mathbf{A}}_{\mathrm{new}} - \widehat{\mathbf{A}}_{\mathrm{old}}\right\| \le \delta \tag{20}$$

$$\min_{\widehat{\mathbf{A}}\in\mathbb{R}^5}\left\|\mathbf{J}^T\left(\widehat{\mathbf{A}}_0\right)\mathbf{J}\left(\widehat{\mathbf{A}}_0\right)\Delta\widehat{\mathbf{A}} + \mathbf{J}\left(\widehat{\mathbf{A}}_0\right)\mathbf{f}\left(\widehat{\mathbf{A}}\right)\right\| \tag{21}$$

where the matrix product $\mathbf{J}^T(\widehat{\mathbf{A}}_0)\mathbf{J}(\widehat{\mathbf{A}}_0)$ can be conveniently pre-calculated. If the trust region algorithm fails to converge to an acceptable solution, one may drop the assumption on constant Jacobian and restart the minimization from the initial guess.

Incidentally, in many cases there is a sufficiently accurate initial guess available. For instance, it may be obtained from a previous run of the method that had explored a similar stress mode, which holds as long as an identical material state was used by the underlying crystal plasticity model. Such condition is frequently fulfilled if one systematically calculates a point-by-point yield locus section (e.g. the section defined by σ_{11}, σ_{22} plane). Yet another example is that the initial guess may be provided by an analytical yield locus model calibrated for a very similar material state.

The generic procedure outlined above can be straightforwardly utilized for determining data points that are commonly used in calibration of analytical yield loci. For instance, uniaxial tension, uniaxial compression and biaxial stress state can be studied. Suppose that the material state variables, such as texture, are expressed in a reference frame defined by the $\mathbf{e}_1$, $\mathbf{e}_2$, $\mathbf{e}_3$

directions. In many practical applications these directions coincide with the rolling direction (RD), transverse direction (TD) and normal direction (ND). Algorithm 1 allows calculating instantaneous r-values and corresponding yield stresses for a sequence of angles defining rotation around $\mathbf{e}_3$ from the $\mathbf{e}_1$ axis.

A similar algorithm (see Algorithm 2) can be used for calculating evolution of the material state under the stress mode $\widehat{\mathbf{U}}^*$. The algorithm provides a convenient way to determine whether the microscopic state (e.g. crystallographic texture) is stable under the imposed stress mode and to estimate how the associated strain rate evolves. In principle, the algorithm splits the deformation path into smaller increments of plastic strain which results from the stress mode $\mathbf{U}^*$, given the microstructural state of the material. The size of increments is specified by the input parameter $\Delta\varepsilon$. At the end of each increment the state of the microstructure is updated to reflect the changes caused by the deformation. Eventually the procedure returns a sequence of triplets $(\varepsilon, \mathbf{A}, \mathbf{S}_H(\mathbf{A}))$. Non-essential operations, such as reporting the history of microstructural state variables, are omitted for clarity.

Suppose one wants to determine the contour of the yield locus. Algorithm 3 presents how the normalized σ_{11},σ_{22} yield locus section can be calculated. The algorithm can be also used for collecting data needed for calculating the Cartesian tangent to the yield locus contour:

$$\frac{d\sigma_{22}}{d\sigma_{11}} = \frac{\frac{dS(\theta)}{d\theta}\sin\theta + S(\theta)\cos\theta}{\frac{dS(\theta)}{d\theta}\cos\theta - S(\theta)\sin\theta} \tag{22}$$

where $S(\theta)$ is the distance from the origin of the coordinate system to the yield locus contour in that section. The polar derivative $dS(\theta)/d\theta$ can be numerically estimated from a single run of Algorithm 3.

Algorithm 1. VEF algorithm for calculating r-values and normalized yield stresses for a sequence of uniaxial loadings defined by directions $\boldsymbol{\alpha}$.

Input: sequence of angles: $\boldsymbol{\alpha} = [\alpha_1, \ldots, \alpha_n]$, stress state: m (either 1 for tension or -1 for compression), accuracy threshold: f_{tol}, logical flag: *reusePrevious*
Result: sequence of triplets $(\alpha, r_\alpha, y_\alpha)$: $\mathbf{o}$

$\boldsymbol{\sigma}_0 \leftarrow m \begin{bmatrix} 1 & 0 & 0 \\ 0 & 0 & 0 \\ 0 & 0 & 0 \end{bmatrix}$
$\mathbf{o} \leftarrow \emptyset$
$hasConverged \leftarrow$ False
foreach α *in* $\boldsymbol{\alpha}$ **do**
  $\mathbf{R} \leftarrow \begin{bmatrix} \cos\alpha & -\sin\alpha & 0 \\ \sin\alpha & \cos\alpha & 0 \\ 0 & 0 & 1 \end{bmatrix}$ `// Rotation matrix`
  $\boldsymbol{\sigma}_r \leftarrow \mathbf{R}^T \boldsymbol{\sigma}_0 \mathbf{R}$
  $\mathbf{S}_r \leftarrow \boldsymbol{\sigma}_r - \frac{1}{3}\operatorname{tr}\boldsymbol{\sigma}_r \mathbf{I}$
  $\mathbf{U}_r^* \leftarrow \dfrac{\mathbf{S}_r}{\|\mathbf{S}_r\|}$
  if *reusePrevious AND hasConverged* **then**
    $\mathbf{A}_0 \leftarrow \mathbf{R}^T \mathbf{A} \mathbf{R}$
  else
    $\hat{\mathbf{A}}_0 \leftarrow \hat{\mathbf{U}}_0$
  end
  $hasConverged \leftarrow$ False
  $\hat{\mathbf{A}}_r^* \leftarrow \underset{\hat{\mathbf{A}} \in \mathbb{R}^5}{\operatorname{argmin}} \|\mathbf{F}(\hat{\mathbf{A}}_r, \hat{\mathbf{U}}_r^*)\|$ given $\hat{\mathbf{A}}_0$ `// see (17)-(21)`
  if $\|\mathbf{F}(\hat{\mathbf{A}}_r^*, \hat{\mathbf{U}}_r^*)\| < f_{\text{tol}}$ **then**
    $hasConverged \leftarrow$ True
    $\mathbf{A} \leftarrow \mathbf{R}\mathbf{A}_r^*\mathbf{R}^T$
    $r_\alpha \leftarrow \frac{\mathbf{A}_{22}}{\mathbf{A}_{33}}$
    $y_\alpha \leftarrow \sqrt{3/2}\|\mathbf{S}_H(\mathbf{A})\|$
    $\mathbf{o} \leftarrow \mathbf{o} + (\alpha, r_\alpha, y_\alpha)$ `// extend the sequence o`
  end
end
return $\mathbf{o}$

Algorithm 2. VEF algorithm for calculating material state evolution under the imposed deviatoric stress mode $\mathbf{U}^*$.

Input: stress mode: $\mathbf{U}^*$, maximal von Mises strain: $\varepsilon_{\max}$, increment of von Mises strain: $\Delta\varepsilon$, accuracy threshold: f_{tol}
Result: sequence of triplets $(\varepsilon, \mathbf{A}, \mathbf{S}_H(\mathbf{A}))$: $\mathbf{o}$

$\boldsymbol{\varepsilon}_{\text{total}} \leftarrow 0$
$\hat{\mathbf{A}}_0 \leftarrow \hat{\mathbf{U}}^*$
$\mathbf{o} \leftarrow \emptyset$
while $\sqrt{2/3}\|\boldsymbol{\varepsilon}_{\text{total}}\| < \varepsilon_{\max}$ **do**
  $\hat{\mathbf{A}}^* \leftarrow \underset{\hat{\mathbf{A}}\in\mathbb{R}^5}{\text{argmin}}\|\mathbf{F}(\hat{\mathbf{A}}, \hat{\mathbf{U}}^*)\|$ given $\hat{\mathbf{A}}_0$ // see (17)-(21)
  if $\|\mathbf{F}(\hat{\mathbf{A}}^*, \hat{\mathbf{U}}^*)\| < f_{\text{tol}}$ **then**
    $\Delta\boldsymbol{\varepsilon} \leftarrow \Delta\varepsilon\mathbf{A}^*$
    $\mathbf{o} \leftarrow \mathbf{o} + (\varepsilon, \mathbf{A}^*, \mathbf{S}_H(\mathbf{A}^*))$ // extend the sequence $\mathbf{o}$
    Update CP state variables by applying $\Delta\boldsymbol{\varepsilon}$
    $\boldsymbol{\varepsilon}_{\text{total}} \leftarrow \boldsymbol{\varepsilon}_{\text{total}} + \Delta\boldsymbol{\varepsilon}$
  else
    return $\mathbf{o}$
  end
end

Algorithm 3. VEF algorithm for calculating scaled σ_{11}, σ_{22} yield locus section.

Input: angular range: θ_0, $\theta_{\max}$, angular resolution: $\Delta\theta$, scaling stress: S_s, shear stress: σ_{12}, logical flag: *reusePrevious*
Result: sequence of pairs $(\theta, S(\theta)/S_s)$: $\mathbf{o}$

$\mathbf{o} \leftarrow \emptyset$
for $\theta = \theta_0$ *to* $\theta_{\max}$ *every* $\Delta\theta$ **do**
  $\boldsymbol{\sigma} \leftarrow \begin{bmatrix} \cos\theta & \sigma_{12} & 0 \\ \sigma_{12} & \sin\theta & 0 \\ 0 & 0 & 0 \end{bmatrix}$
  $\mathbf{S} \leftarrow \boldsymbol{\sigma} - \frac{1}{3}\text{tr}\,\boldsymbol{\sigma}\,\mathbf{I}$
  $\mathbf{U}^* \leftarrow \dfrac{\mathbf{S}}{\|\mathbf{S}\|}$
  if $\theta \neq \theta_0$ *and reusePrevious* **then** $\hat{\mathbf{A}}_0 \leftarrow \hat{\mathbf{A}}^*$
  $\hat{\mathbf{A}}^* \leftarrow \underset{\hat{\mathbf{A}}\in\mathbb{R}^5}{\text{argmin}}\|\mathbf{F}(\hat{\mathbf{A}}, \hat{\mathbf{U}}^*)\|$ given $\hat{\mathbf{A}}_0$ // see (17)-(21)
  $S \leftarrow \|\mathbf{S}_H(\mathbf{A}^*)\|$
  $\mathbf{o} \leftarrow \mathbf{o} + (\theta, \dfrac{S}{S_s})$ // extend the sequence $\mathbf{o}$
end

2.2. Macroscopic plasticity model: the BBC2008 yield criterion

In order to distinguish between the elastic and the plastic state of deformation, a scalar-valued yield function is usually defined:

$$F(\boldsymbol{\sigma}) = \overline{\sigma}(\boldsymbol{\sigma}) - Y \leq 0 \tag{23}$$

where $\overline{\boldsymbol{\sigma}} \geq 0$ is the equivalent yield stress and $Y > 0$ is an arbitrary reference yield stress. The yield surface holds the property that $F(\boldsymbol{\sigma}) = 0$, thus the deformation occurs elasto-plastically, whereas purely elastic stress state satisfies the strict inequality $F(\boldsymbol{\sigma}) < 0$.

The formalism of Equation (23) does not account for the influence of the material state on plastic anisotropy. An extension to the yield criterion can be introduced by adding parameters that depend on the instantaneous material state:

$$F(\boldsymbol{\sigma},\mathbf{z}) = \overline{\sigma}(\boldsymbol{\sigma}) - Y \leq 0 \tag{24}$$

where the vector of parameters $\mathbf{z} = \mathbf{z}(\varepsilon_{pl})$ is derived from the current microscopic state of the material. Therefore, the extended formalism (24) also discards the assumption that the plastic anisotropy does not change during the plastic deformation.

This study extends the BBC2008 yield criterion, which was originally proposed by Comsa and Banabic (2008). The formulas presented below use the formalism provided by Equation (24).

The macroscopic plasticity model makes a constitutive assumption that the material is a plastically orthotropic membrane under plane-stress conditions. Given the plane-stress constraint, the only non-zero components of the Cauchy stress tensor $\boldsymbol{\sigma}$ are σ_{11}, σ_{22} and $\sigma_{12} = \sigma_{21}$. The BBC2008 yield criterion defines the equivalent stress as:

$$\overline{\sigma}(\boldsymbol{\sigma},\mathbf{z}) = \left[(w-1)\sum_{i=1}^{s}\left\{w^{i-1}P(\boldsymbol{\sigma},\mathbf{z}) + w^{s-1}Q(\boldsymbol{\sigma},\mathbf{z})\right\}\right]^{\frac{1}{2k}} \tag{25}$$

$$P(\boldsymbol{\sigma},\mathbf{z}) = \left[L^{(i)}(\boldsymbol{\sigma},\mathbf{z}) + M^{(i)}(\boldsymbol{\sigma},\mathbf{z})\right]^{2k} + \left[L^{(i)}(\boldsymbol{\sigma},\mathbf{z}) - M^{(i)}(\boldsymbol{\sigma},\mathbf{z})\right]^{2k} \tag{26}$$

$$Q(\boldsymbol{\sigma},\mathbf{z}) = \left[M^{(i)}(\boldsymbol{\sigma},\mathbf{z}) + N^{(i)}(\boldsymbol{\sigma},\mathbf{z})\right]^{2k} + \left[M^{(i)}(\boldsymbol{\sigma},\mathbf{z}) - N^{(i)}(\boldsymbol{\sigma},\mathbf{z})\right]^{2k} \tag{27}$$

The coefficient w is defined as $w = (3/2)^{1/s} > 1$, where $s \in \mathbb{N}$. The choice of the exponent k must satisfy the condition that $s \in \mathbb{N}$ to ensure convexity of the yield surface (Comsa and Banabic, 2008). Furthermore, Comsa and Banabic (2008) recommended to use $k = 4$ and $k = 3$ for fcc and bcc materials, respectively. The scalar functions L, M and N are given by:

$$L^{(i)}(\boldsymbol{\sigma},\mathbf{z}) = L^{(i)}(\sigma_{11},\sigma_{22},\mathbf{z}) = l_1^{(i)}(\mathbf{z})\sigma_{11} + l_2^{(i)}(\mathbf{z})\sigma_{22} \tag{28}$$

$$\begin{aligned} M^{(i)}(\boldsymbol{\sigma},\mathbf{z}) &= M^{(i)}(\sigma_{11},\sigma_{22},\sigma_{12},\mathbf{z}) \\ &= \sqrt{\left[m_1^{(i)}(\mathbf{z})\sigma_{11} - m_2^{(i)}(\mathbf{z})\sigma_{22}\right]^2 + \left[m_3^{(i)}(\mathbf{z})(\sigma_{12}+\sigma_{21})\right]^2} \end{aligned} \tag{29}$$

$$\begin{aligned} N^{(i)}(\boldsymbol{\sigma},\mathbf{z}) &= N^{(i)}(\sigma_{11},\sigma_{22},\sigma_{12},\mathbf{z}) \\ &= \sqrt{\left[n_1^{(i)}(\mathbf{z})\sigma_{11} - n_2^{(i)}(\mathbf{z})\sigma_{22}\right]^2 + \left[n_3^{(i)}(\mathbf{z})(\sigma_{12}+\sigma_{21})\right]^2} \end{aligned} \tag{30}$$

Equations (28)–(30) contain several material-dependent parameters, which can be conveniently gathered into the vector:

$$\mathbf{p} = \left\{l_1^{(i)}(\mathbf{z}),\ l_2^{(i)}(\mathbf{z}),\ m_1^{(i)}(\mathbf{z}),\ m_2^{(i)}(\mathbf{z}),\ m_3^{(i)}(\mathbf{z}),\ n_1^{(i)}(\mathbf{z}),\ n_2^{(i)}(\mathbf{z}),\ n_3^{(i)}(\mathbf{z})\ (i = 1,\ldots,s)\right\} \tag{31}$$

Depending on the parameter s, the BBC2008 yield criterion may include 8 components in $\mathbf{p}$ for $s = 1$, 16 components if $s = 2$, 24 components for $s = 3$ and so forth. A simple naming convention will be followed that BBC2008pN stands for the BBC2008 yield criterion comprising N parameters. Throughout this paper we shall exclusively use the BBC2008p16, therefore to find the required 16 parameters, at least the same number of data points has to be found by means of either the virtual or mechanical testing. In the subsequent paragraphs the quantities of experimental nature (even though the experiment might be virtual) are denoted with the superscript '(exp)'.

To identify the parameters in $\mathbf{p}$, Comsa and Banabic (2008) proposed an identification procedure that involves minimization of the following error function:

$$e(\mathbf{p}) = \sum_{\alpha_j}\left[\frac{y_{\alpha_j}^{(\exp)}}{y_{\alpha_j}(\mathbf{p})} - 1\right]^2 + \sum_{\alpha_j}\left[r_{\alpha_j}^{(\exp)} - r_{\alpha_j}(\mathbf{p})\right]^2 + \left[\frac{y_b^{(\exp)}}{y_b(\mathbf{p})} - 1\right]^2 + \left[r_b^{(\exp)} - r_b(\mathbf{p})\right]^2 \tag{32}$$

where y_α are the normalized uniaxial yield stresses and r_α are the corresponding r-values (Lankford coefficients) measured in uniaxial tension tests in the direction α, y_b is the yield stress under equibiaxial tension along RD and TD (Banabic et al., 2005) and r_b is the corresponding equibiaxial r-value (Barlat et al., 2003a). The yield stresses are scaled by the uniaxial yield stress in the RD direction. The formulae for calculating these quantities from the BBC2008 can be found in Comsa and Banabic (2008). Provided that the BBC2008p16 yield criterion is used, the set of data points comprise the same number of measurements as the number of parameters in vector $\mathbf{p}$, i.e. r_0, y_0, r_{15}, y_{15}, …, r_{90}, y_{90}, r_b, and y_b.

It has to be pointed out that the selection of the data points used in that identification procedure is greatly influenced by technical feasibility of conducting relevant mechanical tests. Since the VEF is able to provide data points for virtually any

stress or strain mode, the yield criterion (25) can be calibrated in a much more comprehensive way. In this paper we propose three enhancements to the identification procedure.

Firstly, to generalize the identification procedure, one may redefine the identification problem in such a way that the square norm of the vector-valued error function

$$\mathbf{E}(\mathbf{p}) = \begin{Bmatrix} w_y\mathbf{y}(\mathbf{p}) \\ w_r\mathbf{r}(\mathbf{p}) \\ w_{yb}\mathbf{y}_b(\mathbf{p}) \\ w_{rb}\mathbf{r}_b(\mathbf{p}) \\ w_S\mathbf{S}(\mathbf{p}) \\ w_\beta\boldsymbol{\beta}(\mathbf{p}) \end{Bmatrix} \tag{33}$$

is minimized. This problem can be conveniently solved by means of general non-linear least squares solvers, such as the Levenberg–Marquardt or the Trust Region algorithms. The weighting factors w_y, w_r, w_{yb}, w_{rb}, w_S and w_β allow one to control the relative importance of the individual components. The components of vectors $\mathbf{y}(\mathbf{p})$ and $\mathbf{r}(\mathbf{p})$ include residuals pertaining to the series of n uniaxial tensile tests along angles α_i w.r.t. RD:

$$\mathbf{y}(\mathbf{p}) = \left\{1 - \frac{y(\mathbf{p},\alpha_1)}{y^{(\exp)}(\alpha_1)}, \ldots, 1 - \frac{y(\mathbf{p},\alpha_n)}{y^{(\exp)}(\alpha_n)}\right\}^T \tag{34}$$

$$\mathbf{r}(\mathbf{p}) = \left\{1 - \frac{r(\mathbf{p},\alpha_1)}{r^{(\exp)}(\alpha_1)}, \ldots, 1 - \frac{r(\mathbf{p},\alpha_n)}{r^{(\exp)}(\alpha_n)}\right\}^T \tag{35}$$

where $y^{(\exp)}(\alpha)$ and $y(\mathbf{p},\alpha)$ denote the yield stress calculated in the direction α by the virtual experiments and derived from the yield criterion (25), respectively, while and $r(\mathbf{p},\alpha)$ are the r-values obtained in analogous way. The contribution of the equibiaxial point to the error function is included via terms:

$$\mathbf{y}_b(\mathbf{p}) = \left\{1 - \frac{y_b(\mathbf{p})}{y_b^{(\exp)}}\right\}^T \tag{36}$$

$$\mathbf{r}_b(\mathbf{p}) = \left\{1 - \frac{r_b(\mathbf{p})}{r_b^{(\exp)}}\right\}^T \tag{37}$$

Alas, as in many optimization problems, the uniqueness of the solution can be hardly proved, and many local minima may be encountered. The enhanced formulation (33) improves the identification procedure by introducing new terms $\mathbf{S}(\mathbf{p})$ and $\boldsymbol{\beta}(\mathbf{p})$, which impose additional constraints on the solution. These terms are calculated as follows:

$$\mathbf{S}(\mathbf{p}) = \left\{1 - \frac{S(\mathbf{p},\theta_1)}{S^{(\exp)}(\theta_1)}, \ldots, 1 - \frac{S(\mathbf{p},\theta_m)}{S^{(\exp)}(\theta_m)}\right\}^T \tag{38}$$

$$\boldsymbol{\beta}(\mathbf{p}) = \left\{\cos\left(\beta^{(\exp)}(\theta_1) - \beta_1(\mathbf{p},\theta_1)\right), \ldots, \cos\left(\beta^{(\exp)}(\theta_m) - \beta_m(\mathbf{p},\theta_m)\right)\right\}^T \tag{39}$$

The angle θ defines the ratio between σ_{11} and σ_{22}: $\tan\theta = \sigma_{22}/\sigma_{11}$, while $S(\mathbf{p},\theta)$ is the magnitude of the yield stress in the direction given by the angle θ. The normal to the yield contour and the σ_{11} direction form the angle $\beta(\theta)$. Fig. 1 presents the relations between these quantities in a normalized yield section. The normal direction to the yield locus contour can be readily derived from the tangent to the yield envelope given by Equation (22). From the normality rule, $\beta(\theta)$ corresponds to the direction of the plastic strain rate. In principle, this quantity can be measured experimentally, e.g. Kuwabara et al. (2002), Kuwabara (2007). The data needed by (38)–(39) can be directly calculated by Algorithm 3, which is able to deliver m data points corresponding to biaxial stress state with arbitrary stress ratios.

Another enhancement is added in a less straightforward way. While the basic identification procedure attempts to reduce the number of data points, which has sound justification if the data are acquired by costly mechanical testing, the enhanced version uses more data points than the number of parameters. In other words, the enhanced identification method is formulated as an overdetermined least squares problem. An overdetermined least squares approach was employed in some previous works, e.g. (Rabahallah et al., 2009; Grytten et al., 2008) that focused on identifying the Yld2004 3D yield criterion (Barlat et al., 2005). However, indiscriminate selection of data points was typically used, which resulted in large data sets, varying in size from few thousands (Grytten et al., 2008; Zhang et al., 2015) to tens of thousands of data points (Rabahallah et al., 2009). The present approach reduces the number of virtual experiments by means of a targeted selection. Furthermore, we attempt to maximize the amount of information acquired from the data points by capturing the size of the yield locus and its curvature at the same time.

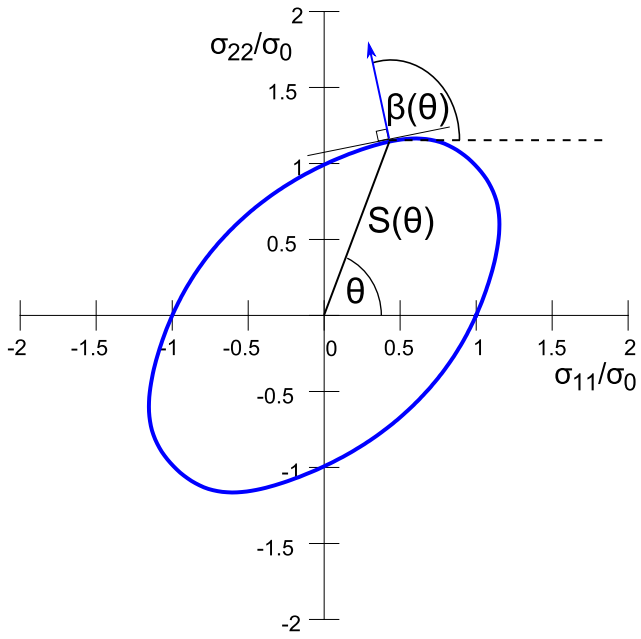

Fig. 1. Schematic illustration of $S(\theta)$ and $\beta(\theta)$ in a normalized yield locus section. The direction of σ_{11} coincides with the RD, while the σ_{22} is parallel to the TD. $S(\theta)$ denotes the distance from the origin to the yield locus, while $\beta(\theta)$ is the angle between the normal to the yield locus and the σ_{11} direction.

When considering possible benefits and overheads associated with the overdetermined problem, one should not overlook the fact that the ultimate purpose of the identification procedure is to be used in an automated way inside the hierarchical multi-scale framework. It can be reasonably argued that strong preference should be given to the method that avoids getting tangled in apparent local minima. Otherwise it would deteriorate the approximation of the crystal plasticity yield surface needed by the macroscopic FE model.

One may expect that some local minima of the function (32) are not necessarily the extreme values of $||\mathbf{E}(\mathbf{p})||$, since the latter uses also other means to assess the quality of the solution. Fig. 2 illustrates such a case. The input data for identification have been gathered by means of the VEF for a deformation texture originating from one of the multi-scale simulations presented in Section 3. In the figure the method that makes use of Equation (32) is referred to as the basic identification, while the enhanced identification avails of the function (33). The two identification procedures have been started from the same initial guess. To localize the minima, the Levenberg–Marquardt algorithm was followed until convergence of good numerical quality. As it is clearly seen in Fig. 2a and b, both methods reached solutions that allow very accurate prediction of the r-values and uniaxial yield stresses over a broad range of directions. Let us now turn to the normalized yield locus sections shown in Fig. 2c. For the sake of argument, the complete contour of the yield locus was determined by the VEF (plotted with the blue line), although only the points marked with symbols have been used by the enhanced identification method. The figure reveals major deviations from the reference yield locus if the basic identification algorithm is used. The discrepancy is particularly notable in the regions that are far away from the uniaxial or equibiaxial stress state. The enhanced version of the procedure results in a clearly superior solution for the simple reason that both the size of the yield surface and its curvature were available to the identification procedure. As a result, the contour of the VEF yield locus (blue line) and the approximation by the BBC2008p16 (green line) almost perfectly coincide.

It is worth mentioning that the contributions from the components (38) and (39) are in many cases complementary. For example, in Fig. 2c the points at $\theta = 135^\circ$ on the blue and red curves are clearly different in terms of the distance $S(\theta)$, yet there is hardly any difference with respect to the angle $\beta(\theta)$. Turning now to $\theta = 15^\circ$, quite the opposite is true: here the deviation with regard to the contour curvature noticeably prevails.

2.3. Criterion for evolution of the BBC2008 anisotropy model

If the yield criterion (25) is incorporated into an explicit time integration FE solver, many small time steps are performed, due to the stability conditions of the time integration scheme. It is quite obvious that a recalculation of the coefficients in (31) at each integration point in every time increment would be highly inefficient. Given small strains associated to the time increments, one may postpone updating the state variables $\mathbf{z}$ and the subsequent recalculation of the coefficients $\mathbf{p} = \mathbf{p}(\mathbf{z})$ until a certain criterion is met at the integration point considered. Once the criterion is fulfilled, an updated vector of coefficients (25) is computed. To do so, evolution of $\mathbf{z}$ along the recent deformation path is calculated by employing the crystal plasticity model, then the VEF is employed to characterize the updated material state, and finally the coefficients of the BBC2008p16 are identified.

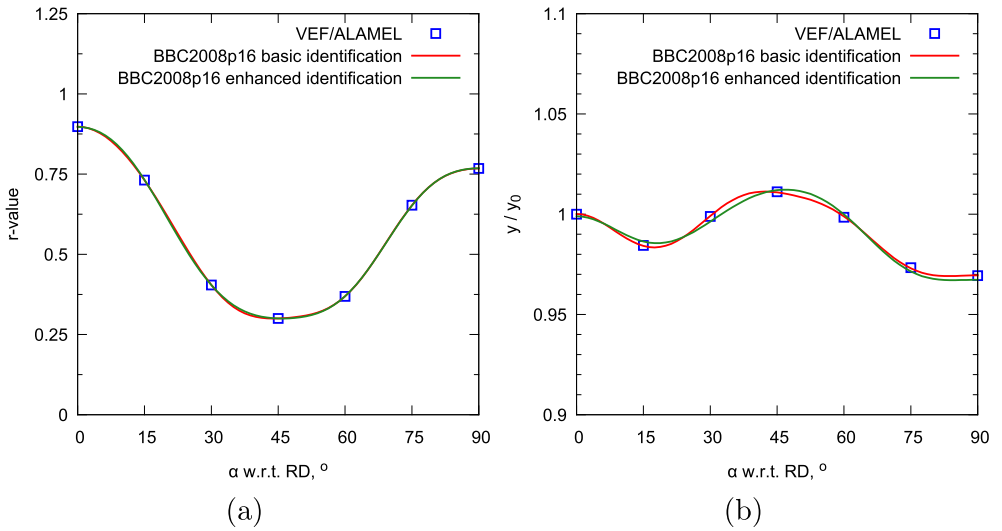

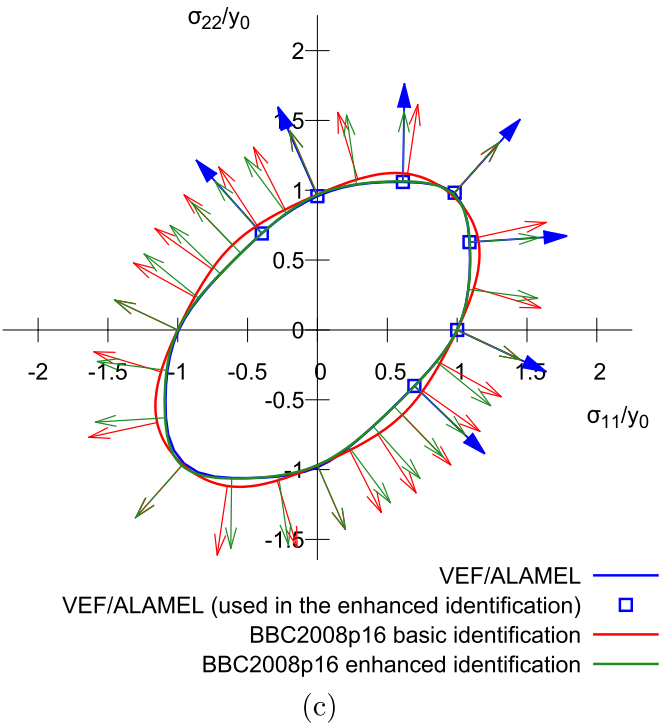

Fig. 2. Comparison of BBC2008p16 calibrated by means of the basic identification procedure (32) and the enhanced procedure, which utilizes (33). Input data points (open symbols) were calculated by the stress-driven VEF according to the ALAMEL homogenization scheme. The normal directions to the yield locus sections are marked with arrows every $\Delta\theta = 15^{\circ}$. The arrows denoting the normals to the VEF/ALAMEL yield locus section are drawn longer merely for a clearer visual appearance.

We choose the update criterion proposed in Gawad et al. (2013), which tracks the plastic strain accumulated since the previous update of the anisotropy model:

$$\mathbf{P} = \int_{t_{i-1}}^{t_i} \mathbf{D}(t)\mathrm{d}t \tag{40}$$

where t_i is the current time since the start of the simulation, and t_{i-1} is the time of the previous update. The tracking is carried out independently at each integration point. Similarly, the decision about the update is made independently from one

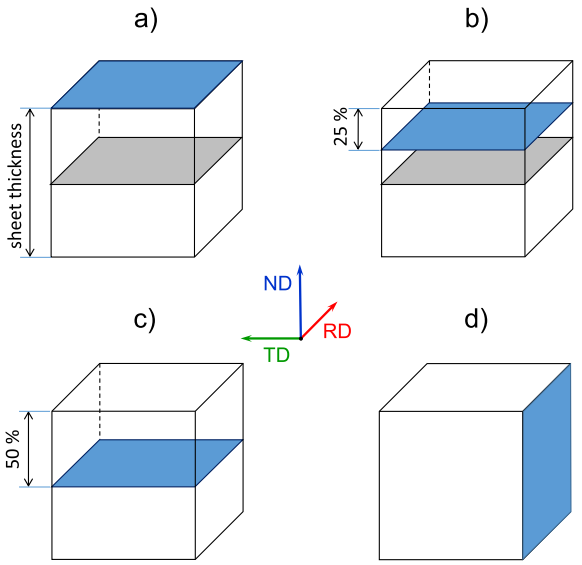

Fig. 3. Schematic sketch of the experimental texture measurement scheme. The blue plane depicts the surface exposed to the X-ray beam: a) surface of the sheet on the RD-TD plane, (0% depth), b) at 25% depth on the RD-TD plane, c) at 50% depth on TD-RD plane, and d) through-thickness on the ND-RD plane. (For interpretation of the references to colour in this figure legend, the reader is referred to the web version of this article.)

integration point to another. When the norm of this accumulated plastic strain exceeds a critical value (i.e. $||\mathbf{P}|| \geq P_{cr}$), both the microstructural state variables and the anisotropy model at the integration point are updated.

3. Results

3.1. Characterization of the initial material

The material used in this study was an AA6016-T4 metallic sheet (1 mm nominal thickness). This material is a precipitation hardening alloy, containing aluminium, magnesium and silicon as major components. The metallic sheet has been delivered in the T4 status (solution heat treated and naturally aged).

3.1.1. Measurements of the initial texture

The crystallographic texture was measured by means of X-ray diffraction. The samples were cut out of the original sheet in a location close to its longitudinal axis. Three depths across the sheet thickness were reached by means of grinding: 0% (which corresponds to the surface of the sheet), 25% and 50%. Additionally, the through-thickness texture was measured. The measurements are schematically depicted in Fig. 3. In the subsequent part of the paper we use the following naming convention for the texture data with respect to their origin: texture A, B, C and D denote texture at 0%, 25%, 50% depths and the average through-thickness, respectively.

The $\phi_2 = 45^\circ$ sections of the ODFs, as well as the values of the Texture Index (TI) are shown in Fig. 4. Firstly, let us consider the group of ODFs measured at different depths. It is clear just from the texture index values that a complex texture gradient

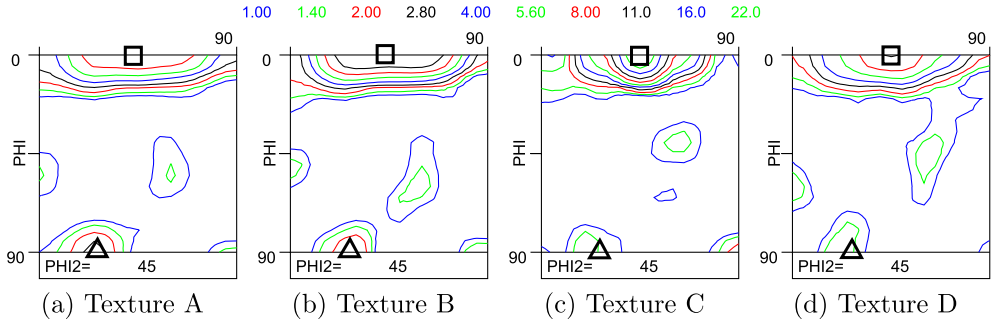

Fig. 4. $\phi_2 = 45^\circ$ ODF sections (with ϕ_1 and Φ on horizontal and vertical axis, respectively) of the experimental textures: a)–c) measured at different depth in thickness direction: a) 0% depth, TI = 2.75, b) 25% depth, TI = 3.95 and c) 50% depth, TI = 4.96 and d) through-thickness texture, TI = 2.45. Annotations indicate the Cube component (square) and the P component (triangle). The ODFs are expressed in identical reference frame: x_1 = RD, x_2 = TD and x_3 = ND.

exists across the thickness. The gradient is not limited to the overall intensity, but it also manifests itself in the intensities of individual texture components. Generally, the texture tends to sharpen towards the mid-plane of the sheet, which is mostly attributed to the Cube component, i.e. the orientation given by $(\phi_1,\Phi,\phi_2) = (45^\circ,0^\circ,45^\circ)$ in this ODF section. Moreover, the spread around Cube forms a fibre towards $(45^\circ + x,0^\circ,45^\circ)$ and $(45^\circ - x,0^\circ,45^\circ)$. For texture A, the Cube fibre is pronounced and 'complete', i.e. $x = 45^\circ$. At the mid-plane however, the Cube fibre is only partial, i.e. $x < 45^\circ$. In the ODF section in Fig. 4 also the P texture component $(29.5^\circ,90^\circ,45^\circ)$ can be identified. The P component is generally attributed to the recrystallization solutionizing annealing (Engler and Hirsch, 2002). In the investigated material the P component intensifies from the mid-plane towards the surface of the sheet. The analysed textures contain also some minor Goss component $\{011\}\langle 100\rangle$, which is seen in this section as a small intensity maximum at $(\phi_1,\Phi,\phi_2) = (90^\circ,90^\circ,45^\circ)$. At this point we can conclude that the mid-plane texture C (Fig. 4c) does not seem to be representative for the entire volume of the material, since it is much sharper than the textures A and B.

Passing on now to the texture measured over the thickness of the sheet, it is remarkable that it is the least intense in terms of texture index. Similarly as it was seen in the textures A and B, the Cube fibre is well developed. However, the P component is barely present, analogously as it was found in texture C.

3.1.2. Determination of the mechanical parameters

In order to determine the uniaxial mechanical parameters, tensile tests were performed on specimens cut at 0°, 15°, 30°, 45°, 60°, 75°, and 90° from the rolling direction. The experiments were carried out using a Zwick-Roell 150 kN universal tensile testing machine equipped with an extensometer with 20 mm gauge-length. Fig. 5 summarizes the results of uniaxial tensile tests.

The coefficients of Swift hardening law

$$\overline{\sigma}(\varepsilon_{vM}) = K(\varepsilon_{vM} + \varepsilon_0)^n \tag{41}$$

were determined from the average of the uniaxial tests as $K = 479.7$ MPa, $n = 0.239$ and $\varepsilon_0 = 0.00096$. All the multi-scale simulations presented in the subsequent sections used the same macroscopic isotropic hardening model, thus the experimental hardening curves in Fig. 5 were not directly exploited.

The tensile tests also provided the values of the conventional yield stress $y = R_{p0.2}$ and the Lankford coefficients r associated to the previously mentioned directions (see Fig. 6a and b). The measured r-values reflect the plastic anisotropy at the beginning of yield.

The mechanical response of the metallic sheet in biaxial tension regime was studied by means of hydraulic bulging and thickness compression tests. The hydraulic bulging experiments allowed determining the balanced biaxial yield stress according to the methodology described by Lazarescu et al. (2011). The thickness compression tests were performed to determine the biaxial coefficient of plastic anisotropy (Barlat et al., 2003a). The balanced biaxial yield stress was found $y_{bx} = 160.1$ MPa, while the measurement of the biaxial coefficient of plastic anisotropy resulted in $r_{bx} = 1.037$ (cf. Fig. 6c).

3.1.3. Characterization of initial anisotropy by virtual experiments

To summarize the previous subsection, the four samples are quite dissimilar with respect to important texture features. Thus, it is difficult to assess which one is truly representative of the entire sheet. To answer this question, we verified whether the apparent differences in the microstructural features were eventually reflected in the properties of interest, namely in the plastic anisotropy. The study was not restricted to ascertaining whether the properties are initially congruent, but also how the properties would evolve under certain loadings.

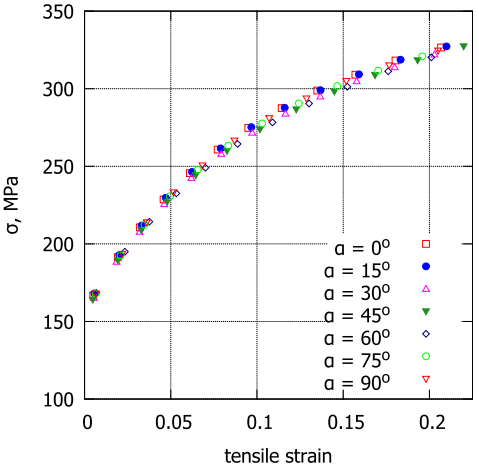

Fig. 5. Results of the uniaxial tensile tests performed along different directions α w.r.t RD in the plane of the sheet.

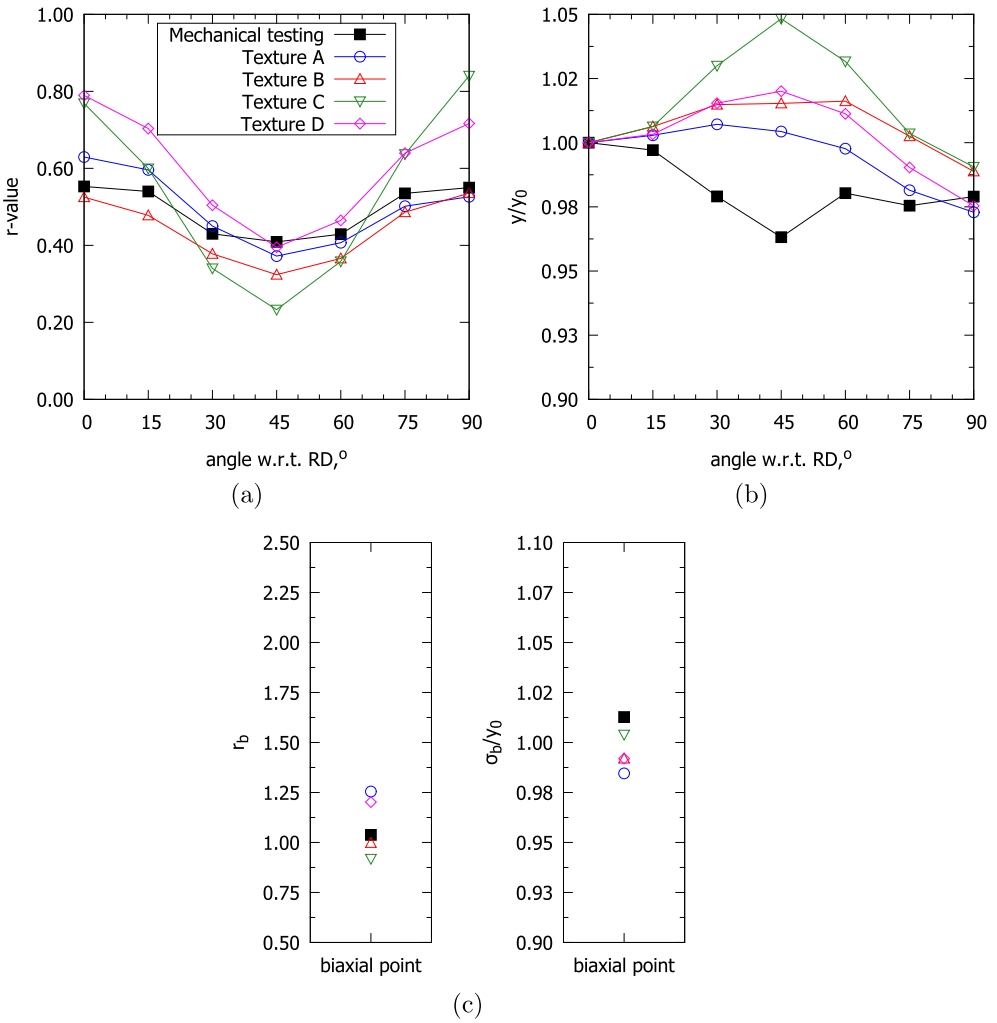

Fig. 6. Initial characterization of plastic anisotropy obtained by means of the mechanical testing and virtual experiments: a) Lankford coefficient (r-value), b) uniaxial yield stress and c) biaxial yield stress and r-values. All yield stresses are scaled by the uniaxial yield stress along 0° to RD. The legend in (a) applies to all the plots. The initial experimental textures (cf. Fig. 4) A, B, C and D were used in the virtual experiments.

The textures A–D were used as input data to virtual experiments. The first step in setting up the virtual experiments was to calculate discrete ODFs, needed by the ALAMEL model. The orientations were probed from the continuous ODFs using the STAT algorithm described in Tóth and Van Houtte (1992) and implemented in the MTM-FHM software (Van Houtte, 1995). Each of the initial data sets consisted of $N = 5000$ crystallographic orientations, expressed as Euler angles in Bunge (1982) convention: ϕ_1, Φ and ϕ_2.

In the remaining part of the paper we will consistently use the ALAMEL model by Van Houtte et al. (2005) as the basic constituent of the virtual experimentation framework presented in Section 2.1. The same model will be used for predicting both texture evolution and associated changes to the plastic anisotropy. Identical critical resolved shear stresses will be assumed on all 12 $\{111\}\langle 110\rangle$ slip systems.

The VEF was used for calculating the data points needed for identification of the BBC2008 yield criterion. Fig. 6 presents the calculated r-values and the yield stresses along with the results of the mechanical testing. It can be seen from Fig. 6 that the r-values resulting from the mechanical testing are in a good consistency with the outcomes from the virtual experiments, in particular with the one based on the surface texture A. However, this is not the case if other quantities are considered. In terms of the scaled uniaxial yield stresses, the VEF and the mechanical tests predict opposite trends: the maximum around 45° is consistently obtained in all virtual experiments, whereas the mechanical testing resulted in a minimum in this direction. As it can be seen in Fig. 6b, the variability of the experimental normalized uniaxial yield stress is bound in the range of ($\approx$0.97, 1.0), therefore only a minor fluctuation of $\approx$3% is present. This limited variability can also be noticed in Fig. 5. Therefore, it is perfectly possible that the experimental result does not fully reflect the actual material behaviour, since every measurand includes certain measurement uncertainty. At this point it remains debatable whether the crystal plasticity or the mechanical experiment provides better estimate of the actual material behaviour in the considered case.

Another prominent difference between the mechanical and the virtual testing is found in the biaxial yield stresses. Apart from the discrepancy in magnitude, the crystal plasticity predicts very limited variation. This is consistent with the yield locus sections calculated by the VEF (see the equibiaxial point in Fig. 7a).

The textures A and C seem to be associated with quite dissimilar anisotropic features, which is most visible in the biaxial ratio r_b: the respective values appear as the outliers in the plot. Fig. 7a provides a firm confirmation of this observation: the relevant yield locus contours are clearly different in curvature at the biaxial tension point.

Moreover, the texture C results in much more pronounced anisotropy under uniaxial loading in comparison to the textures A, B and D (Fig. 6a–c). This is likely attributed to the Cube fibre in the texture. The complete and relative homogeneous Cube fibre observed in the texture A (Fig. 4a) decreases the dependency of both the r-value and the yield stress with respect to the loading direction. In contrast, the partial and inhomogeneous Cube fibre in the texture C (Fig. 4c) results in a relatively large dependency on uniaxial loading direction.

Let us now examine the evolution of r-values under uniaxial tensile loading shown in Fig. 8. The virtual tests allow much larger strains than usually achievable in their mechanical counterparts. It seems to be a common pattern that the uniaxial tension along RD and TD have hardly any influence on the strain contraction ratio. Another trend is identified that the increase in strain decreases the directionality of the properties in question. This is visible in the reduction in the vertical spread of the evolution lines, and at the same time directing towards $r = 1$ that corresponds to isotropy. With the exception of texture B, the loading along the directions approx. 45° w.r.t. RD results in the most rapid change in terms of the r-value.

To summarize, the data presented suggest a texture gradient across the thickness, which is accompanied by an even more distinctive gradient in anisotropy. Broadly speaking, texture A (at the surface of the sheet) and texture C (at 50% of sheet thickness) form two extrema with respect to the texture features and the plastic anisotropy. It can be conclusively stated that the texture measured at the mid-plane of the sheet thickness should not be considered a representative sample of the material. However, no pivotal evidence has been gathered so far to indicate which of the other three should be preferred. For this reason all four textures A–D will be used in the remaining part of the study.

3.2. Cup drawing test

The experimental part of the cup drawing benchmark included forming of cylindrical cups from circular blanks. The circular blank of diameter 90 mm and 1 mm thickness was deformed in an adopted Erichsen device. The following dimensions characterize the geometry of the tools: punch diameter: 50 mm, punch lip radius: 6 mm, die diameter: 52.82 mm and die lip radius: 3 mm. The experiment was repeated twice. After the deep drawing, cup profiles were measured and averaged over symmetrically equivalent positions.

The corresponding cup drawing simulations were performed using the Abaqus Explicit FEA code. Due to the symmetry of the process, one-quarter of the blank was simulated. To accelerate the computations, a mass scaling procedure was used, although quasi-static conditions were ensured. The blank was discretized using 3247 reduced integration wedge continuum shell elements (in Abaqus nomenclature: SC6R). Although only one layer of elements was used, the elements were set to include 3 integration points across the thickness. Gaussian integration rule was employed for thickness integration. Frictional contact between the blank and the tools (punch, die and blankholder) was controlled using Coulomb law with the coefficient of friction $\mu = 0.2$, which approximately corresponds to conditions in a lubricated steel-aluminium contact pair.

The BBC2008 criterion was identified for the textures A–D using the data presented in Figs. 6 and 7. In all four cases the BBC2008 was able to nearly ideally reproduce the calibration data. Concerning the setup of the virtual experiments, the

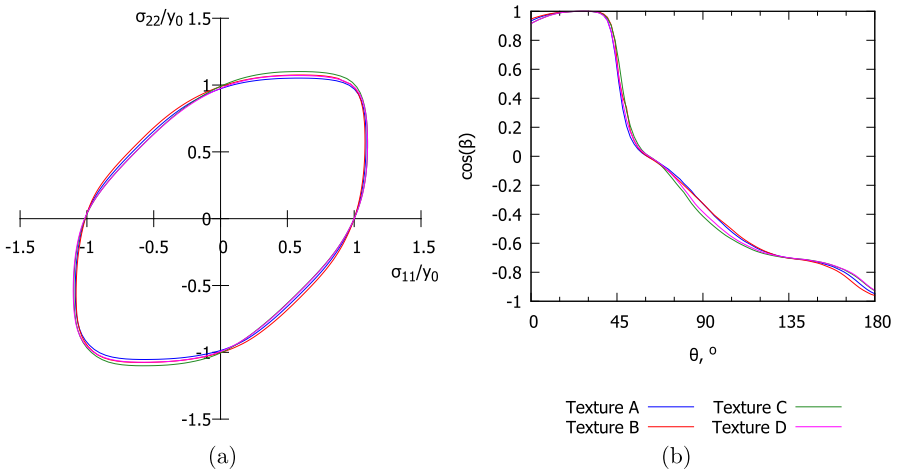

Fig. 7. Initial characterization of plastic anisotropy calculated by virtual experiments: (a) normalized yield locus section, (b) cosines of the angle between the σ_{11} direction and the normal direction to the yield locus contour. The legend in subfigure (b) applies to both plots.

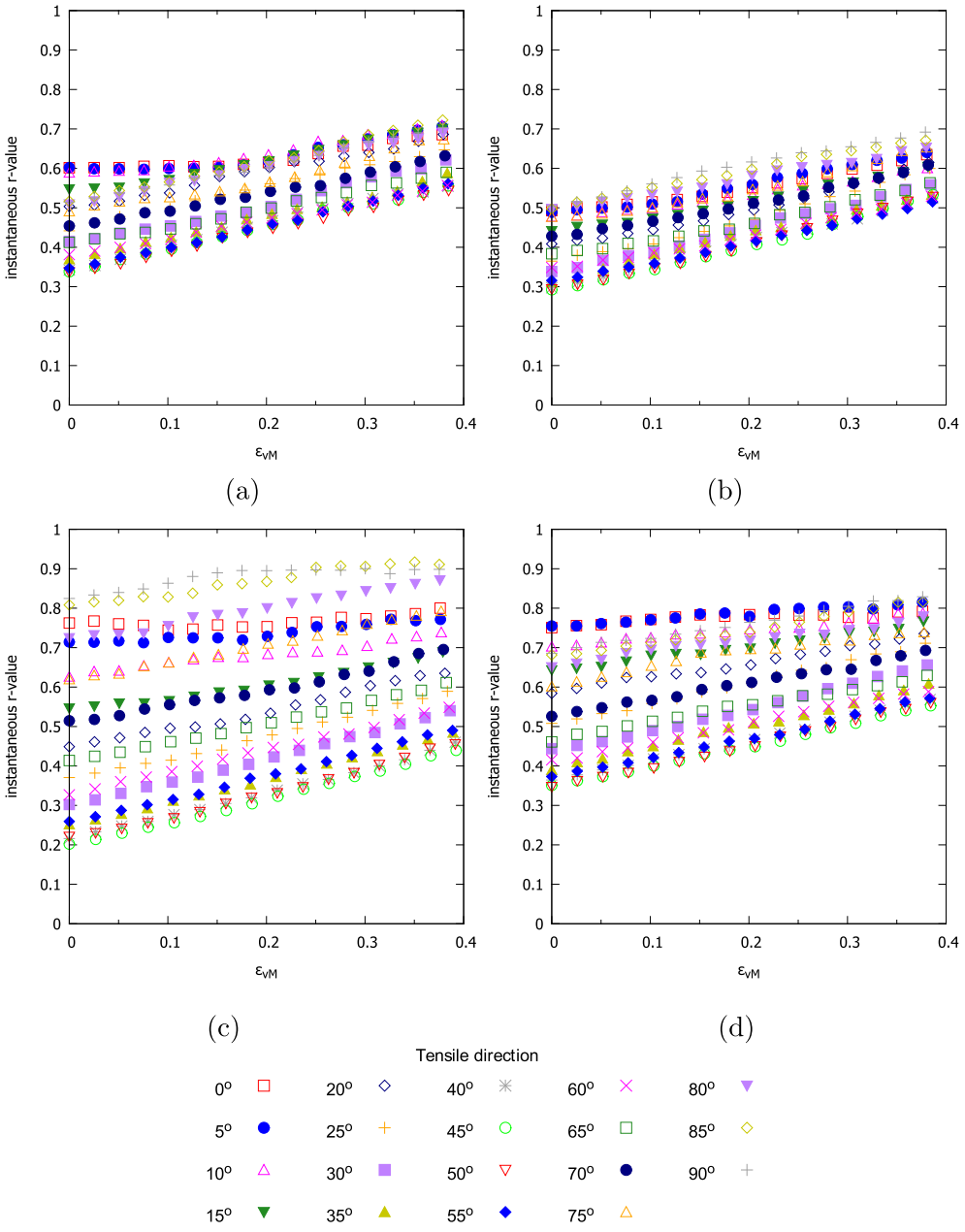

Fig. 8. Evolution of instantaneous *r*-values predicted by a series of virtual uniaxial tensile tests along different directions w.r.t. RD. starting from (a) Texture A, (b) Texture B, (c) Texture C and (d) Texture D.

directions of uniaxial loading were chosen as $\alpha = 0°, 15°, \ldots, 90°$ (cf. (34)–(35)) and the following directions θ were used in (38)–(39) to define biaxial stress ratios: 7°, 30°, 45°, 60°, 83°, 120° and 330°. The point evaluated at $\theta = 45°$ was also used in Equations (36)–(37) for calculating the r_b and y_b. The identical selection of data points was used in the simulations exploiting the HMS-BBC2008 model. All the weighting factors in (33) were set to unity, except for $w_\beta = 4$.

We performed two groups of multi-scale simulations. In the first group, the BBC2008 criterion was calibrated with the VEF data shown in Fig. 6 and kept constant throughout the simulation. The second group employed the HMS-BBC2008 model. The simulations started from the textures presented in Fig. 4 and the corresponding VEF data points for calibration, but subsequently the texture and the anisotropy model have been regularly updated according to the criterion presented in Section 2.3. The updating of the texture and the yield locus model was independently triggered in each integration point every 0.05 of plastic strain accumulated since the previous update. In addition to the multi-scale simulations, an FE simulation was carried out with the BBC2008 yield criterion identified using the results of the mechanical testing (see Fig. 6). Another FE simulation with the same hardening behaviour and Abaqus built-in isotropic von Mises plasticity model was conducted as a reference solution.

The computations were carried out on an HPC cluster. The HMS-BBC2008 simulations were executed on ten 12-core Westmare nodes. On average it took 5 h for an HMS-BBC2008 simulation to complete, while the corresponding BBC2008 simulation required 1 h on a single node.

The results of the simulations and experiments are summarized in Fig. 9. Generally, the total cup height is consistently underestimated by all the models considered, including the isotropic one. It is also remarkable that the FE mesh itself introduces some artificial anisotropy, which produces spurious irregularities of the cup profile simulated with the isotropic material model (see Fig. 9a). A similar pattern of aberrations is observed in all other cases.

To elucidate possible origins of the discrepancy with respect to the total cup height, a parametric study was conducted by varying the hardening parameters and the friction coefficient. The gap between the experiment and simulation was bridged only by combinations of the parameters that lack sound physical grounds: either very high friction or much softer material had to be assumed. Since the discrepancy was systematically observed in all test cases, including the one employing von Mises isotropy, one might presume that either the FE discretization or the plane stress assumption is responsible for the underestimated cup height. To explore the former hypothesis, the discretization by means of conventional shell elements (S4R) was tested in several variants, howbeit without any significant improvement observed.

Although none of the simulations perfectly reproduces the experimental profile, it is clear that the texture-based simulations deliver superior predictions of the earing behaviour. While the simulations based on the virtual experiments result in correctly positioned ears, the modelling that relies on mechanical testing wrongly predicts the ears at 45° w.r.t. RD. The

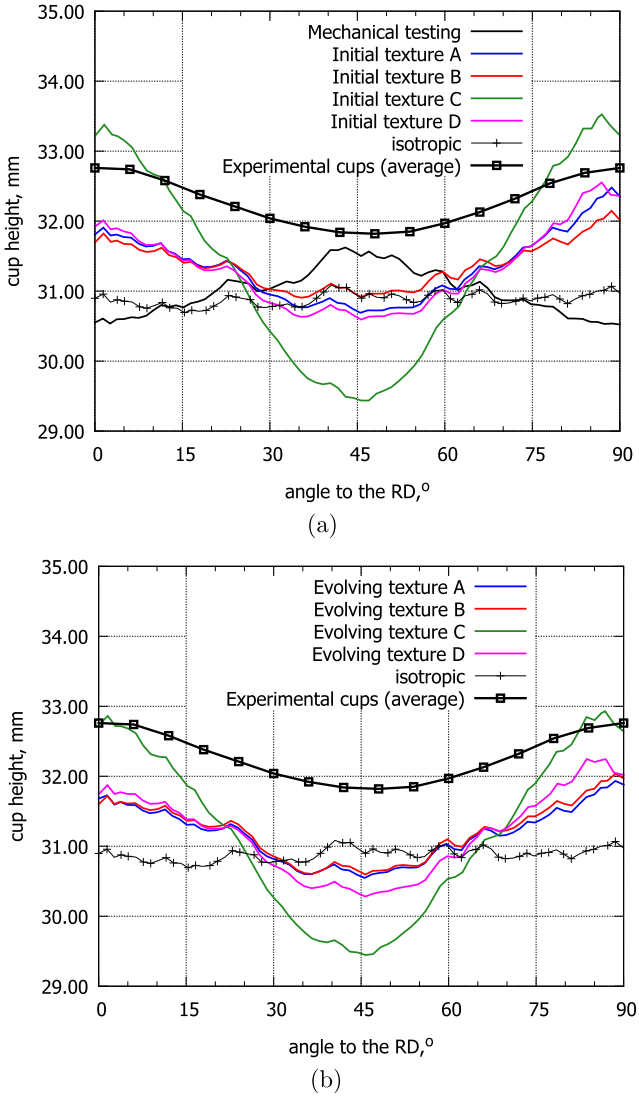

Fig. 9. Comparison of experimental and predicted cup profiles: a) constant anisotropy models, b) evolving anisotropy HMS-BBC2008. Results for a simple isotropic model are added as a reference.

discrepancy can be partly explained if we recall the most significant distinction between the mechanical testing and the texture-based virtual experiments found in Figs. 6 and 7. In contrast to the virtual tests, the mechanical testing resulted in a minimum of uniaxial yield stresses in the direction around 45° w.r.t. RD. This minimum appears to be a factor associated with the position of the valley, for the reason that it corresponds to decreased resistance to tension in that direction.

The stress state in the flange, nevertheless, considerably differs from uniaxial tension. Depending on the radial position in the flange, it may vary from nearly pure compression along the circumferential direction (at the outer rim) to a superposition of tension along the radial direction and predominant compression along the circumference. Suppose the Cauchy stress is expressed in a cylindrical coordinate system given by the axes ($\mathbf{e}_r$, $\mathbf{e}_\psi$, $\mathbf{e}_z$). The origin of the coordinate system is fixed and coincides with the centre of the blank, while the axes correspond to the radial direction of the blank, angular position along the circumference and the sheet normal, respectively. One may use the radial stress σ_{rr} and tangential stress $\sigma_{\psi\psi}$ to approximately characterize the instantaneous stress state in the flange by means of the ratio

$$s = \frac{\sigma_{rr}}{\sigma_{\psi\psi}} \tag{42}$$

provided that $\sigma_{zz} \approx 0$. The plastic flow, which is a consequence of the stress state, can be then described by the ratio

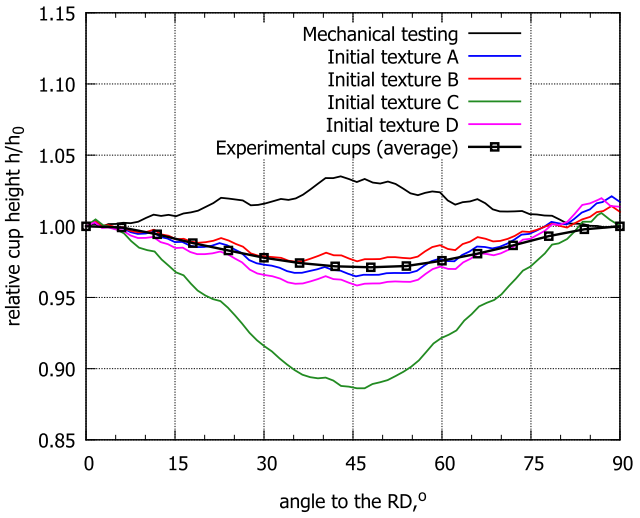

(a)

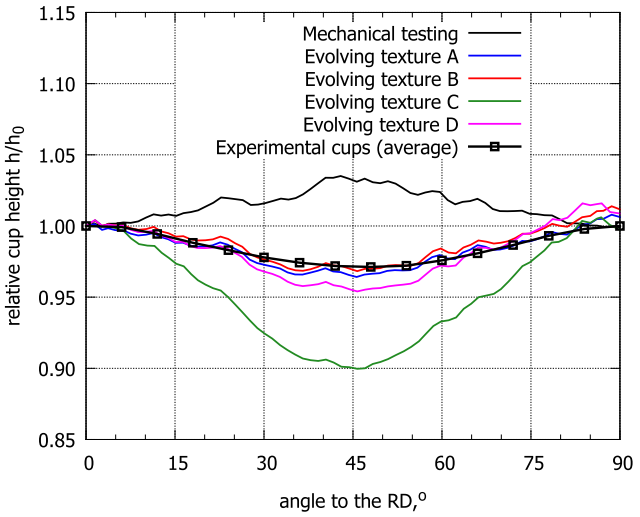

(b)

Fig. 10. Comparison of experimental and predicted relative cup profiles, scaled by cup height at 0° w.r.t. RD: a) constant anisotropy models, b) evolving anisotropy HMS-BBC2008.

$$e = \frac{\varepsilon_{rr}}{\varepsilon_{\psi\psi}} \tag{43}$$

between the radial and tangential strains (ε_{rr} and $\varepsilon_{\psi\psi}$, respectively). Since the strain components are in a direct relation with the yield locus through the strain rates calculated from the normality rule, the e-ratio depends on the yield locus shape as well.

Fig. 11 shows the s-ratio and e-ratio calculated for a subset of the considered cup drawing simulations. For the sake of clarity, the figure includes just the results of the simulations that are based on mechanical testing, virtual experiments for texture A and the HMS-BBC2008 evolving anisotropy started from texture A. The strain evolution of the s-ratio and the corresponding e-ratio was tracked in three finite elements, initially located at identical radius $r = 40$ mm along the RD, TD and 45° w.r.t. RD. The strain range was chosen to ensure that the considered material points remain sufficiently far from the die lip, and at the same time $\sigma_{zz} \approx 0$. As can be seen in Fig. 11a, the stress state is not only quite distinct from the uniaxial tension, but it also varies with increasing plastic strain. As a direct consequence, different points on the yield locus are probed.

Let us now compare the resulting characteristics of material flow shown in Fig. 11b. The most pronounced difference between the two crystal plasticity based simulations and the one based on the mechanical testing data is visible at the RD and TD locations. Despite certain variation in the s-ratio within the considered group of simulations, the stress state is dominantly imposed by the geometry of the process. This particularly holds at the onset of the plastic deformation, when the stress state in the given coordinate system remains nearly identical in all the cases. Thus, the divergence in the material flow is most likely attributed to the shape of the explored yield locus regions. It appears that the relatively limited deviation from the uniaxial tension state results in probing the yield surface in regions of remarkably different curvature.

If the yield locus model is calibrated primarily to the uniaxial tension data, as it is the case if the mechanical testing data are used, the regions of the yield locus that are actually reached in the cup drawing simulation are relatively distant from the measurement points. On the contrary, the yield loci derived from the virtual experiments are constructed by exploiting data points of various stress ratios, thus one may expect these yield loci to be more reliable, since the stress states relevant to the cup drawing are sampled.

Fig. 11b also reveals the effect of the anisotropy evolution on the material flow. The strain history of the e-ratio coincides in the texture-based simulations only until the very first update of the yield locus. The least abrupt change in the flow direction is seen in the material point at the RD.

Another aspect of the cup geometry prediction is related to the intensity of texture used as the starting point. As it could be anticipated from Fig. 6, the sharpest texture (texture C) resulted in excessively pronounced ears. Other texture-based predictions of the ear height are generally correct. This can be more easily demonstrated in Fig. 10, which presents the cup heights divided by h_0 being the height of each cup at RD. Surprising as it may seem, the BBC2008 calibrated to virtual experiments with the surface texture A and the texture B provide slightly more accurate ear profile prediction than the one based on the average texture D (see Fig. 9a).

In comparison with the constant anisotropy model, the HMS-BBC2008 simulations generally improve cup prediction by decreasing ear height, as it is shown in Fig. 9b). With the only exception of the simulation initialized with the sharpest texture

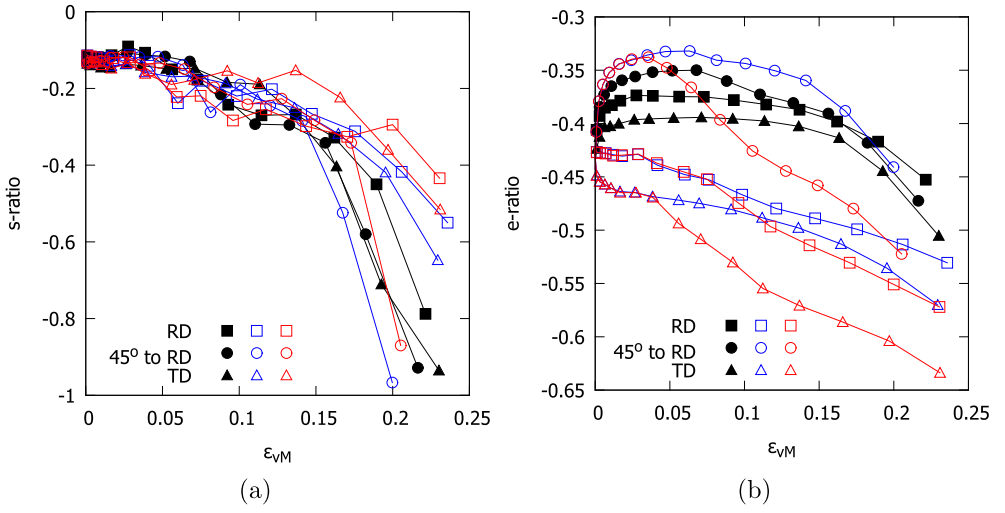

Fig. 11. Evolution of a) s-ratio and b) e-ratio as a function of equivalent von Mises plastic strain in the cup drawing simulations at selected points in the flange: RD, 45° to RD and TD. The simulations use the yield loci constructed from the mechanical testing data (black), VEF data for the initial texture A (blue) and the HMS-BBC2008 evolution from texture A (red), respectively. (For interpretation of the references to colour in this figure legend, the reader is referred to the web version of this article.)

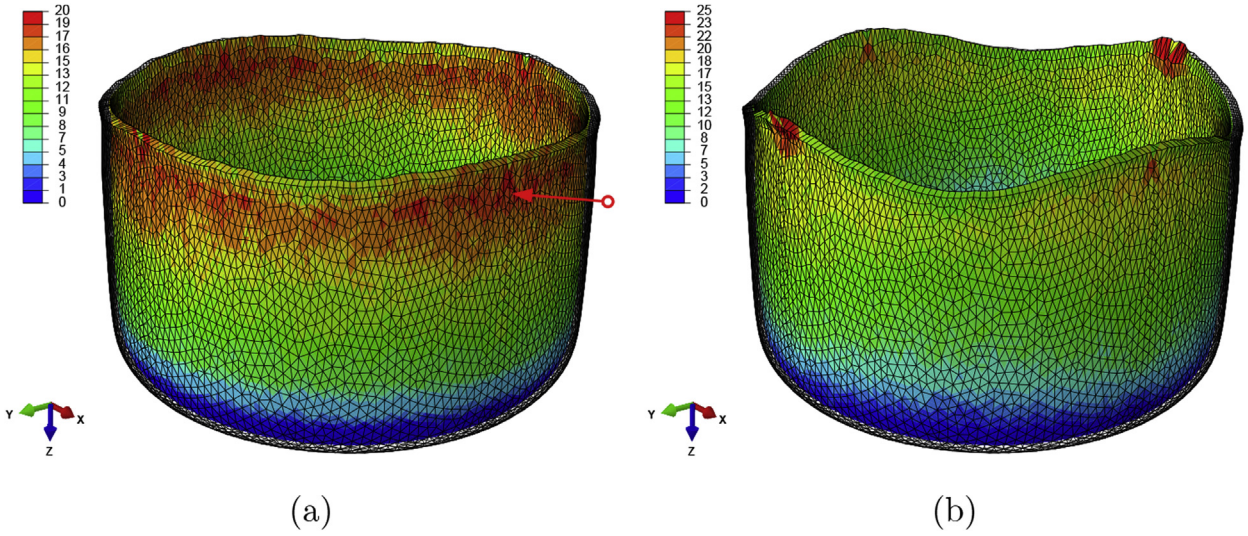

Fig. 12. Number of updates of texture and anisotropy, presented as a field projected on the final cups: a) Texture A and b) Texture C are used as the initial textures (symmetries on the XZ and YZ planes are superimposed). The arrow indicates the position of the selected integration point approx. 3 mm away from the cup rim at the RD.

(texture C), the experimental and calculated cup profiles show very good agreement. Moreover, in terms of the relative ear height profile, the predictions started from textures A, B and D are generally accurate. The least visible effect of anisotropy evolution is seen if the least intense texture D is used.

Admittedly, the anisotropy evolution led to a minor improvement to the cup profiles. The most visible effect of anisotropy evolution is seen in the HMS-BBC2008 simulation starting from texture C, which improved the prediction of cup profile by decreasing the height of the ears at 0° and 90° w.r.t RD. Another noticeable change introduced by anisotropy evolution is that the simulations starting from texture A and texture B result in nearly identical cups, while the respective simulations with constant anisotropy showed differences at 45° and 90°. Yet again, the correction due to anisotropy evolution improves the relative cup profiles in these two cases, which are eventually in almost perfect agreement with the experimental cups (see Fig. 10).

Let us now take a closer look how the fine-scale material state evolves and to what extent it impacts the planar anisotropy. Fig. 12 presents an example of simulated cups with a superimposed field showing the count of anisotropy updates. As it can be expected from Equation (40), the field variable is tightly correlated with the magnitude of the plastic strain. The regions of the highest plastic strain have been updated multiple times, thus one might expect that not only the texture but also the anisotropic properties shall be far from the initial ones. Fig. 13 summarises the r-values and the uniaxial yield stresses that correspond to the final predicted textures evolved from textures A–D in the geometrical location shown in Fig. 12a. The figure compares the results of the virtual experiments and the BBC2008 approximation that was locally reconstructed from the virtual experiment data. With regard to the effects of texture evolution on the plastic behaviour under uniaxial loading, the r-values are moderately affected. Much more complex evolution is observed when the uniaxial yield stresses are examined. Those not only tend to decrease, but the monotonicity is influenced as well: the maximum at direction 45° in the initial material clearly diminishes (cf. Fig. 6), with the exception for the sharpest texture D.

Another observation is that in terms of the uniaxial r-values and the yield stresses, the properties of texture B and texture D generally evolve in a remarkably similar way. The corresponding lines in Figs. 6a and 13a remain almost parallel. By the same token, the uniaxial yield stresses in Fig. 13b exhibit much similar variation.

We can conclude from Fig. 13 that the BBC2008p16 not only reproduces the VEF data remarkably well, but it is also generally capable of following the changing anisotropy in a repeatable and consistent manner. This is also confirmed in Fig. 14, which illustrates the anisotropy evolution[2] during the cup drawing in the location pointed out in Fig. 12a. All the yield stresses in the figure are scaled by the instantaneous uniaxial yield stress in tension along the RD. It is seen in the figure that while in terms of the r-values the material gradually evolves towards more isotropic behaviour, the directionality of the uniaxial yield stresses generally increases. The shape of the yield locus is affected as well, which is also reflected in the evolution of the equibiaxial r-value r_b and the corresponding equibiaxial yield stress. While the size of the yield locus at the equibiaxial point

[2] Animated figure is available in the supplementary data related to this article. Please see the online version at http://dx.doi.org/10.1016/j.ijplas.2015.02.011.

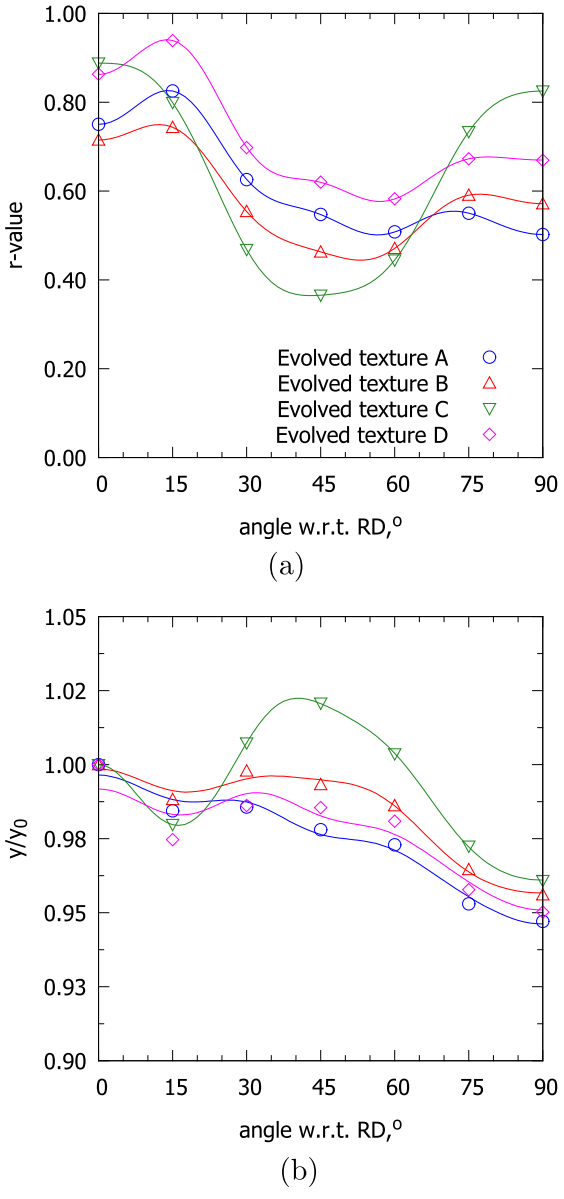

Fig. 13. a) r-values and b) scaled uniaxial yield stresses calculated from evolved textures in the simulated fully formed cups: ALAMEL-based virtual experiments (filled symbols), BBC2008 local yield locus calibrated to the virtual experiments (lines). The legend in a) applies to both plots.

evolves slowly, the changes in the yield locus shape occur more rapidly. This explains the fast variation in the r_b, since it is derived from the plastic strain rate being the normal to the yield locus.

It is remarkable that the subsequent recalibrations smoothly and accurately adapt the macroscopic yield criterion to the changes in the VEF data. Albeit the uniaxial yield stresses show discrepancies in the final stages of the evolution, all other quantities of interest, including the shape of the yield contour given by its normals, are congruently reproduced. This also proves the robustness of the enhanced identification algorithm that utilizes Equation (33).

Yet, one cannot but wonder why the evolution of texture and anisotropy introduced only a minor change to the macroscopic prediction. So far we have seen that the quality of cup profile prediction was already high when texture-derived BBC2008 was used, but the question remains what was the impact of the deformation on the texture evolution. To shed some light on this issue, let us inspect the final deformation textures that the HMS-BBC2008 model predicted. The ODF sections of the textures that evolved in the location shown in Fig. 12a and the corresponding values of texture index are presented in Fig. 15. The ODFs are plotted in the coordinate system coinciding with the material corotational reference frame. A visual inspection reveals a substantial change from the initial ODFs shown in Fig. 4. Even though the Cube component remains the most intense texture feature, a new texture component is regularly found. The Cu (Copper) component {112}

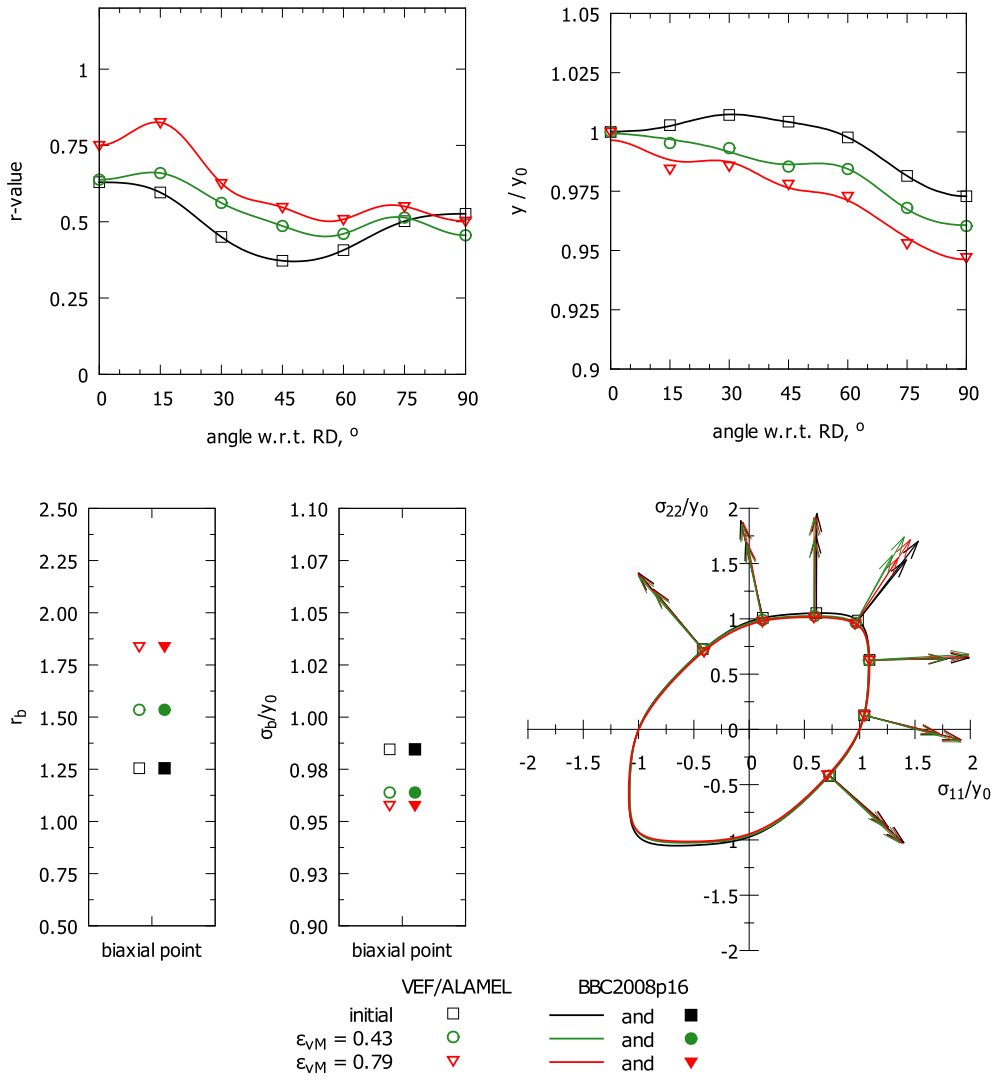

Fig. 14. Evolution of plastic anisotropy during the cup drawing at the material point shown in Fig. 12a. Texture A is used as the starting point. The material point undergoes plastic deformation of $\varepsilon_{vM} \approx 0.79$. For an improved visual appearance the arrows denoting the normals to the VEF/ALAMEL yield locus section are drawn longer. An animated figure is available in supplementary data related to this article. It can be found online at http://dx.doi.org/10.1016/j.ijplas.2015.02.011.

⟨111⟩ of varying intensity emerges in all the analysed textures, most remarkably in the evolved texture D, where it appears almost equally pronounced as the Cube component. Interestingly, the Goss component remains at similar intensity level as it used to be in the initial textures.

The texture index of all the evolved textures is not only systematically lower than in the initial ones, but also less diversified, which suggests the evolved textures become more similar to each other. With this idea in mind, a quantitative comparison of the textures was conducted. The following error function quantifies the difference between a pair of ODFs $f_1(g)$ and $f_2(g)$ given in the three-dimensional space of orientations:

$$\Delta(f_1, f_2) = \int \left[f_1(g) - f_2(g)\right]^2 \mathrm{d}g \tag{44}$$

where $g \in \mathbb{R}^3$. The result of the comparison is illustrated as a heatmap in Fig. 16. The figure can be interpreted as follows: the upper-left triangle contains pairwise differences between the textures in the initial material, while the lower-right triangle shows the differences after the cup drawing operation. Each field on the diagonal represents the difference between the initial texture and the one that evolved from it during the deformation. From the asymmetry of the heatmap one may conclude that the differences between the evolved textures are much lower than it was found in the initial material. The evolved texture C remains the most distinct among the analysed textures. Furthermore, it has undergone the most significant change from its

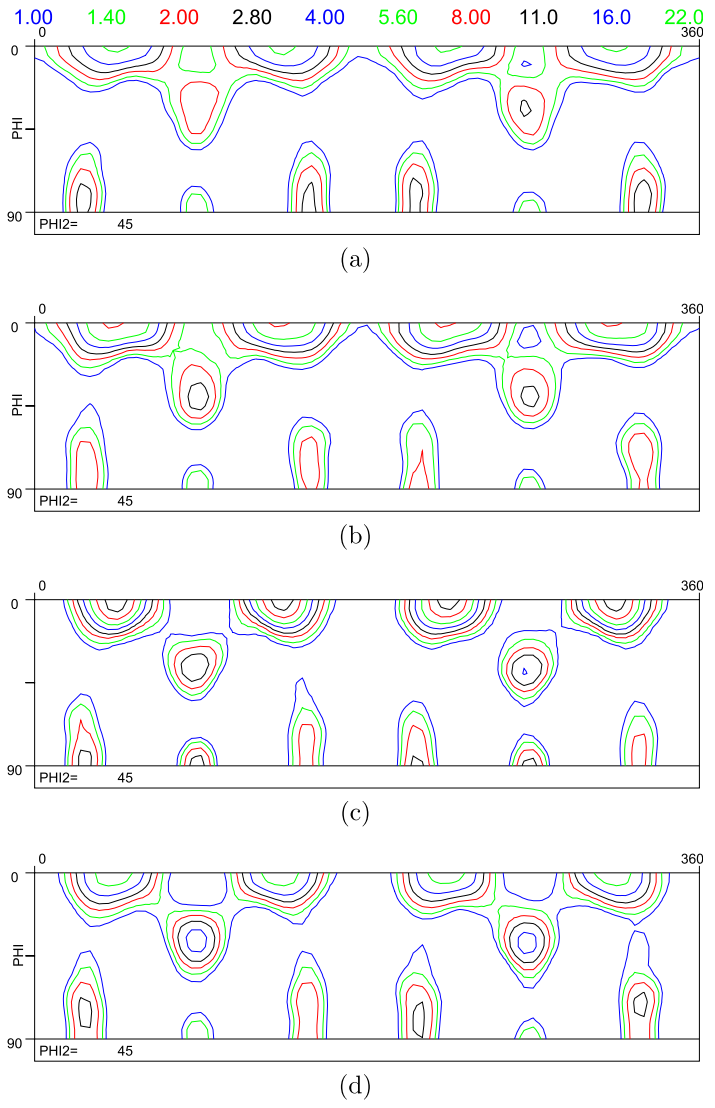

Fig. 15. $\phi_2 = 45^\circ$ ODF sections (with ϕ_1 and Φ on the horizontal and the vertical axis, respectively) of the final texture textures that evolved from: (a) Texture A (TI = 2.06), (b) Texture B (TI = 2.35), (c) Texture C (TI = 3.05), and (d) Texture D (TI = 2.26) in the position indicated in Fig. 12a. All the sections are presented in the identical corotational reference frame, which initially was given by x_1 = RD, x_2 = TD and x_3 is the normal to the sheet.

initial state. In comparison, texture A experienced the least profound evolution, however texture D has changed to a similar extent. Yet the most striking finding that emerges from Fig. 16 is that the differences between the initial textures are in many cases more severe than the changes in texture due to the deformation in the cup drawing (cf. the diagonal and the upper-left triangle of the heatmap). On the other hand, the drawing process results in an increasing similitude between the textures A–D, which can be explained by the fact that they are subjected to nearly identical deformation paths.

4. Conclusions

1. The HMS-BBC2008 model allows capturing evolution of plastic anisotropy that occurs in a sheet metal subjected to plastic deformation. To achieve this, the macroscopic FE model includes a local yield criterion in each integration point. The coefficients of the BBC2008 yield criterion co-evolve with the local crystallographic texture. The changes in the local plastic anisotropy are implemented by systematic reconstruction of the BBC2008, where the calibration data are gathered by virtual experiments.
2. An enhanced identification procedure is proposed for the BBC2008 yield criterion. The main improvement is attributed to in-depth exploitation of data points on the yield locus contour. The identification procedure uses not only the size of the yield locus, but also its local curvature. As a result, the identification algorithm is more robust and less sensitive to local

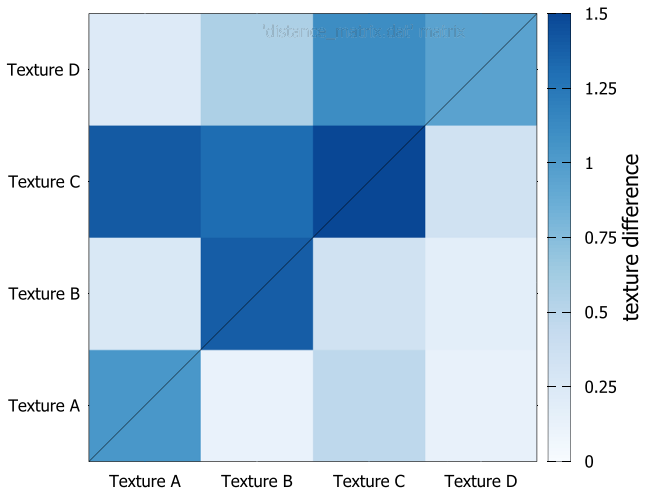

Fig. 16. Quantitative pairwise differences between the analysed textures. Upper-left triangle: differences with respect to the initial material. Lower-right triangle: differences after the cup drawing operation. Diagonal: initial texture versus deformation texture.

minima of the objective function. This generic feature is particularly useful in case of yield criteria that contain a large number of adjustable parameters.

3. The simulations based on the crystal plasticity predictions of anisotropy resulted in substantially more accurate cup profiles (with minimum cup heights at 45° to RD as in the experiments) compared to the simulation relying on the mechanical testing (giving the maximum at 45° to RD).
4. If the cup drawing process of AA6016-T4 aluminium sheet is considered, anisotropy evolution appears to have only a minor effect on the macroscopic geometry of the cup. The results confirm that the texture and anisotropy considerably depart from the initial state, yet the macroscopic effect of the evolution is hardly visible.
5. The presence of a texture gradient in the initial material presents difficulties in selecting a proper representative texture. It was found that the mid-sheet texture is not automatically representative for the sheet behaviour. The average through-thickness texture does not appear to be the optimal choice, either. Surprisingly, more accurate predictions in terms of the macroscopic sample geometry were obtained when any of the near-the-surface textures was chosen. However, the macroscopic effects of a sub-optimal choice can be to some extent alleviated if anisotropy evolution is taken into account.

Acknowledgements

JG, AVB, PE, PVH and DR gratefully acknowledge the financial support from the Knowledge Platform M2Form, funded by IOF KU Leuven, and from the Belgian Federal Science Policy agency, contracts IAP7/19 and IAP7/21. The computational resources and services used in this work were provided by the VSC (Flemish Supercomputer Center), funded by the Hercules Foundation and the Flemish Government – department EWI. DB, DSC and MG gratefully acknowledge the financial support from the PCCE 100 project funded by CNCS.

Appendix A. Vector notation for symmetric traceless second-order tensors

This appendix presents formulas for conversion from second-order tensors of deviatoric nature into five-dimensional vectors (Van Houtte and Van Bael, 2004).

If a symmetric, second-order tensor $\mathbf{x}$ has the property that $\mathbf{x}_{11}+\mathbf{x}_{22}+\mathbf{x}_{33}=0$, then it can be completely described by only five independent components. This property is commonly found in tensors used in mechanics; for instance, deviatoric stresses and plastic strain rates belong to this category. The components of the corresponding 5D vector $\hat{\mathbf{x}}$ can be calculated as:

$$\hat{\mathbf{x}}_1 = \frac{1}{\sqrt{2}}(\mathbf{x}_{11}-\mathbf{x}_{22}) \tag{A.1}$$

$$\hat{\mathbf{x}}_2 = -\sqrt{\frac{3}{2}}\mathbf{x}_{33} \tag{A.2}$$

$$\hat{\mathbf{x}}_3 = \sqrt{2}\mathbf{x}_{23} \tag{A.3}$$

$$\widehat{\mathbf{x}}_4 = \sqrt{2}\mathbf{x}_{31} \tag{A.4}$$

$$\widehat{\mathbf{x}}_5 = \sqrt{2}\mathbf{x}_{12} \tag{A.5}$$

It is trivial to convert back the 5D vector into the second-order tensor:

$$\mathbf{x}_{11} = \frac{1}{\sqrt{2}}\widehat{\mathbf{x}}_1 + \frac{1}{\sqrt{6}}\widehat{\mathbf{x}}_2 \tag{A.6}$$

$$\mathbf{x}_{22} = -\frac{1}{\sqrt{2}}\widehat{\mathbf{x}}_1 + \frac{1}{\sqrt{6}}\widehat{\mathbf{x}}_2 \tag{A.7}$$

$$\mathbf{x}_{33} = -\sqrt{\frac{2}{3}}\widehat{\mathbf{x}}_2 \tag{A.8}$$

$$\mathbf{x}_{23} = \mathbf{x}_{32} = \frac{1}{\sqrt{2}}\widehat{\mathbf{x}}_3 \tag{A.9}$$

$$\mathbf{x}_{31} = \mathbf{x}_{13} = \frac{1}{\sqrt{2}}\widehat{\mathbf{x}}_4 \tag{A.10}$$

$$\mathbf{x}_{12} = \mathbf{x}_{21} = \frac{1}{\sqrt{2}}\widehat{\mathbf{x}}_5 \tag{A.11}$$

It can be easily shown that the scalar product is preserved, i.e. $\mathbf{x} : \mathbf{x} = \widehat{\mathbf{x}} \cdot \widehat{\mathbf{y}}$. As a corollary, the length of the vector $\widehat{\mathbf{x}}$ is equal to the magnitude of the corresponding tensor $\mathbf{x}$.

Other variants of the transformation exist in the literature, see e.g. (Lequeu et al., 1987; Van Houtte, 1988; Grytten et al., 2008).

References

An, Y., Vegter, H., Carless, L., Lambriks, M., 2011. A novel yield locus description by combining the Taylor and the relaxed Taylor theory for sheet steels. Int. J. Plast. 27 (11), 1758–1780.

Aretz, H., Barlat, F., 2012. Unconditionally convex yield functions for sheet metal forming based on linear stress deviator transformation. Key Eng. Mater. 504–506, 667–672.

Aretz, H., Barlat, F., 2013. New convex yield functions for orthotropic metal plasticity. Int. J. Non-Linear Mech. 51, 97–111.

Aretz, H., Hopperstad, O.S., Lademo, O.-G., 2007. Yield function calibration for orthotropic sheet metals based on uniaxial and plane strain tensile tests. J. Mater. Process. Technol. 186 (1–3), 221–235.

Arminjon, M., Bacroix, B., 1991. On plastic potentials for anisotropic metals and their derivation from the texture function. Acta Mech. 88 (3–4), 219–243.

Arul Kumar, M., Mahesh, S., Parameswaran, V., 2011. A 'stack' model of rate-independent polycrystals. Int. J. Plast. 27 (6), 962–981.

Asaro, R., Needleman, A., 1985. Overview no. 42 texture development and strain hardening in rate dependent polycrystals. Acta Metall. 33, 923–963.

Banabic, D., Aretz, H., Comsa, D.S., Paraianu, L., 2005. An improved analytical description of orthotropy in metallic sheets. Int. J. Plast. 21 (3), 493–512.

Banabic, D., Barlat, F., Cazacu, O., Kuwabara, T., 2010. Advances in anisotropy and formability. Int. J. Mater. Form. 3 (3), 165–189.

Banabic, D., Comsa, D., Balan, T., 2000. A new yield criterion for orthotropic sheet metals under plane stress conditions. In: The 7th Conference TPR2000. Cluj Napoca, pp. 217–224.

Banabic, D., Kuwabara, T., Balan, T., Comsa, D.S., Julean, D., 2003. Non-quadratic yield criterion for orthotropic sheet metals under plane-stress conditions. Int. J. Mech. Sci. 45 (5), 797–811.

Barlat, F., Aretz, H., Yoon, J., Karabin, M., Brem, J., Dick, R., 2005. Linear transformation-based anisotropic yield functions. Int. J. Plast. 21 (5), 1009–1039.

Barlat, F., Becker, R.C., Hayashida, Y., Maeda, Y., Yanagawa, M., Chung, K., Brem, J.C., Lege, D.J., Matsui, K., Murtha, S.J., Hattori, S., 1997a. Yielding description for solution strengthened aluminum alloys. Int. J. Plast. 13 (4), 385–401.

Barlat, F., Brem, J., Yoon, J., Chung, K., Dick, R., Lege, D., Pourboghrat, F., Choi, S.-H., Chu, E., 2003a. Plane stress yield function for aluminum alloy sheets – part 1: theory. Int. J. Plast. 19 (9), 1297–1319.

Barlat, F., Duarte, J.M.F., Gracio, J.J., Lopes, A.B., Rauch, E.F., 2003b. Plastic flow for non-monotonic loading conditions of an aluminum alloy sheet sample. Int. J. Plast. 19 (8), 1215–1244.

Barlat, F., Gracio, J.J., Lee, M.-G., Rauch, E.F., Vincze, G., 2011. An alternative to kinematic hardening in classical plasticity. Int. J. Plast. 27 (9), 1309–1327.

Barlat, F., Ha, J., Grácio, J.J., Lee, M.-G., Rauch, E.F., Vincze, G., 2013. Extension of homogeneous anisotropic hardening model to cross-loading with latent effects. Int. J. Plast. 46, 130–142.

Barlat, F., Lege, D.J., Brem, J.C., 1991. A six-component yield function for anisotropic materials. Int. J. Plast. 7 (7), 693–712.

Barlat, F., Maeda, Y., Chung, K., Yanagawa, M., Brem, J.C., Hayashida, Y., Lege, D.J., Matsui, K., Murtha, S.J., Hattori, S., Becker, R.C., Makosey, S., 1997b. Yield function development for aluminum alloy sheets. J. Mech. Phys. Solids 45 (11–12), 1727–1763.

Barlat, F., Vincze, G., Grácio, J., Lee, M.-G., Rauch, E., Tomé, C., 2014. Enhancements of homogenous anisotropic hardening model and application to mild and dual-phase steels. Int. J. Plast. 58, 201–218.

Barlat, F., Yoon, J., Cazacu, O., 2007. On linear transformations of stress tensors for the description of plastic anisotropy. Int. J. Plast. 23, 876–896.

Barton, N.R., Knap, J., Arsenlis, A., Becker, R., Hornung, R.D., Jefferson, D.R., 2008. Embedded polycrystal plasticity and adaptive sampling. Int. J. Plast. 24 (2), 242–266.

Bate, P., 1999. Modelling deformation microstructure with the crystal plasticity finite-element method. Philos. T. Roy. Soc. A 375, 1589.

Bishop, J., Hill, R., 1951a. A theoretical derivation of the plastic properties of a face-centred metal. Philos. Mag. 42, 1298–1307.

Bishop, J., Hill, R., 1951b. A theory of the plastic distortion of a polycrystalline aggregate under combined stresses. Philos. Mag. 42, 414–427.

Bunge, H., 1982. Texture Analysis in Materials Science. Butterworth, London.

Cazacu, O., Barlat, F., 2004. A criterion for description of anisotropy and yield differential effects in pressure-insensitive metals. Int. J. Plast. 20 (11), 2027–2045.
Cazacu, O., Plunkett, B., Barlat, F., 2006. Orthotropic yield criterion for hexagonal closed packed metals. Int. J. Plast. 22 (7), 1171–1194.
Comsa, D., Banabic, D., 2008. Plane-stress yield criterion for highly-anisotropic sheet metals. In: Numisheet 2008, Interlaken, pp. 43–48.
Conn, A.R., Gould, N.I.M., Toint, P.L., 2000. Trust-region methods. SIAM Soc. Ind. Appl. Math..
Crumbach, M., Pomana, G., Wagner, P., Gottstein, G., 2001. Taylor type deformation texture model considering grain interaction and material properties. Part I – fundamentals. In: Gottstein, G., Molodov, D. (Eds.), Proceedings of the 1st Joint International Conference on Recrystallisation and Grain Growth. Springer, Berlin, pp. 1053–1060.
Eisenlohr, P., Diehl, M., Lebensohn, R., Roters, F., 2013. A spectral method solution to crystal elasto-viscoplasticity at finite strains. Int. J. Plast. 46, 37–53.
Engler, O., Crumbach, M., Li, S., 2005. Alloy-dependent rolling texture simulation of aluminium alloys with a grain-interaction model. Acta Mater. 53 (8), 2241–2257.
Engler, O., Hirsch, J., 2002. Texture control by thermomechanical processing of AA6xxx Al–Mg–Si sheet alloys for automotive applications – a review. Mat. Sci. Eng. A 336 (1–2), 249–262.
Eyckens, P., Mulder, H., Gawad, J., Vegter, H., Roose, D., van den Boogaard, T., Van Bael, A., Van Houtte, P., 2015. The prediction of differential hardening behaviour of steels by multi-scale crystal plasticity modelling. Int. J. Plast. http://dx.doi.org/10.1016/j.ijplas.2014.12.004.
Galán, J., Verleysen, P., Lebensohn, R.A., 2014. An improved algorithm for the polycrystal viscoplastic self-consistent model and its integration with implicit finite element schemes. Model. Simul. Mater. Sci. Eng. 22 (5), 055023.
Gawad, J., Van Bael, A., Eyckens, P., Samaey, G., Van Houtte, P., Roose, D., 2013. Hierarchical multi-scale modeling of texture induced plastic anisotropy in sheet forming. Comp. Mater. Sci. 66, 65–83.
Gawad, J., Van Bael, A., Eyckens, P., Van Houtte, P., Samaey, G., Roose, D., 2010. Effect of texture evolution in cup drawing predictions by multiscale model. Steel Res. Int. 81, 1430–1433 (Supplement Metal Forming).
Grytten, F., Holmedal, B., Hopperstad, O., Børvik, T., 2008. Evaluation of identification methods for YLD2004-18p. Int. J. Plast. 24 (12), 2248–2277.
He, W., Zhang, S., Prakash, A., Helm, D., 2014. A hierarchical multi-scale model for hexagonal materials taking into account texture evolution during forming simulation. Comp. Mater. Sci. 82, 464–475.
He, W., Zhang, S., Song, H., 2013. An extended homogenous yield function based anisotropic hardening model for description of anisotropic hardening behavior of materials. Int. J. Mech. Sci. 77, 343–355.
Hill, R., 1948. A theory of the yielding and plastic flow of anisotropic metals. Proc. Roy. Soc. Lond. A193, 281–297.
Hosford, W., 1979. On yield loci of anisotropic cubic metals. In: Proceedings of the 7th North American Metalworking Conf. (NMRC), SME, Dearborn, MI, pp. 191–197.
Inal, K., Mishra, R.K., Cazacu, O., 2010. Forming simulation of aluminum sheets using an anisotropic yield function coupled with crystal plasticity theory. Int. J. Solids Struct. 47 (17), 2223–2233.
Izadbakhsh, A., Inal, K., Mishra, R.K., 2012. Crystal plasticity based finite element modelling of large strain deformation in AM30 magnesium alloy. Model. Simul. Mater. Sci. Eng. 20 (3), 035016.
Kim, D., Barlat, F., Bouvier, S., Rabahallah, M., Balan, T., Chung, K., 2007. Non-quadratic anisotropic potentials based on linear transformation of plastic strain rate. Int. J. Plast. 23 (8), 1380–1399.
Kim, J.H., Lee, M.-G., Barlat, F., Wagoner, R., Chung, K., 2008. An elasto-plastic constitutive model with plastic strain rate potentials for anisotropic cubic metals. Int. J. Plast. 24 (12), 2298–2334.
Knap, J., Barton, N.R., Hornung, R.D., Arsenlis, A., Becker, R., Jefferson, D.R., 2008. Adaptive sampling in hierarchical simulation. Int. J. Numer. Methods Eng. 76 (4), 572–600.
Knezevic, M., Lebensohn, R.A., Cazacu, O., Revil-Baudard, B., Proust, G., Vogel, S.C., Nixon, M.E., 2013. Modeling bending of α-titanium with embedded polycrystal plasticity in implicit finite elements. Mater. Sci. Eng. A 564, 116–126.
Kowalczyk, K., Gambin, W., 2004. Model of plastic anisotropy evolution with texture-dependent yield surface. Int. J. Plast. 20 (1), 19–54.
Kraska, M., Doig, M., Tikhorimov, D., Raabe, D., Roters, F., 2009. Virtual material testing for stamping simulations based on polycrystal plasticity. Comp. Mater. Sci. 46, 383–392.
Kuwabara, T., 2007. Advances in experiments on metal sheets and tubes in support of constitutive modeling and forming simulations. Int. J. Plast. 23 (3), 385–419.
Kuwabara, T., Bael, A.V., Iizuka, E., 2002. Measurement and analysis of yield locus and work hardening characteristics of steel sheets with different r-values. Acta Mater. 50 (14), 3717–3729.
Kuwabara, T., Sugawara, F., 2013. Multiaxial tube expansion test method for measurement of sheet metal deformation behavior under biaxial tension for a large strain range. Int. J. Plast. 45, 103–118.
Lazarescu, L., Comsa, D.S., Banabic, D., 2011. Analytical and experimental evaluation of the stress-strain curves of sheet metals by hydraulic bulge test. Key Eng. Mater. 473, 352–359.
Lebensohn, R.A., 2001. N-site modeling of a 3D viscoplastic polycrystal using fast Fourier transform. Acta Mater. 49 (14), 2723–2737.
Lebensohn, R.A., Kanjarla, A.K., Eisenlohr, P., 2012. An elasto-viscoplastic formulation based on fast Fourier transforms for the prediction of micromechanical fields in polycrystalline materials. Int. J. Plast. 32–33, 59–69.
Lebensohn, R.A., Tomé, C., 1993. A self-consistent anisotropic approach for the simulation of plastic deformation and texture development of polycrystals: application to zirconium alloys. Acta Metall. Mater. 41, 2611–2624.
Lebensohn, R.A., Tomé, C.N., Castañeda, P.P., 2007. Self-consistent modelling of the mechanical behaviour of viscoplastic polycrystals incorporating intra-granular field fluctuations. Philos. Mag. 87 (28), 4287–4322.
Lequeu, P., Gilormini, P., Montheillet, F., Bacroix, B., Jonas, J., 1987. Yield surfaces for textured polycrystals-I. Crystallographic approach. Acta Metall. 35 (2), 439–451.
Mahesh, S., 2010. A binary-tree based model for rate-independent polycrystals. Int. J. Plast. 26 (1), 42–64.
Mánik, T., Holmedal, B., 2013. Additional relaxations in the Alamel texture model. Mat. Sci. Eng. A 580, 349–354.
Mánik, T., Holmedal, B., 2014. Review of the Taylor ambiguity and the relationship between rate-independent and rate-dependent full-constraints Taylor models grain interaction model. Int. J. Plast. 55, 152–181.
Molinari, A., Ahzi, S., Kouddane, R., 1997. On the self-consistent modeling of elastic-plastic behavior of polycrystals. Mech. Mater. 26, 43–62.
Nixon, M.E., Cazacu, O., Lebensohn, R.A., 2010a. Anisotropic response of high-purity α-titanium: experimental characterization and constitutive modeling. Int. J. Plast. 26 (4), 516–532.
Nixon, M.E., Lebensohn, R.A., Cazacu, O., Liu, C., 2010b. Experimental and finite-element analysis of the anisotropic response of high-purity [alpha]-titanium in bending. Acta Mater. 58 (17), 5759–5767.
Peirce, D., Asaro, R., Needleman, A., 1982. An analysis of nonuniform and localized deformation in ductile single crystals. Acta Metall. 30 (6), 1087–1119.
Plunkett, B., Cazacu, O., Barlat, F., 2008. Orthotropic yield criteria for description of the anisotropy in tension and compression of sheet metals. Int. J. Plast. 24 (5), 847–866.
Plunkett, B., Lebensohn, R., Cazacu, O., Barlat, F., 2006. Anisotropic yield function of hexagonal materials taking into account texture development and anisotropic hardening. Acta Mater. 54 (16), 4159–4169.
Prakash, A., Lebensohn, R.A., 2009. Simulation of micromechanical behavior of polycrystals: finite elements versus fast Fourier transforms. Model. Simul. Mater. Sci. Eng. 17 (6), 064010.
Rabahallah, M., Balan, T., Bouvier, S., Bacroix, B., Barlat, F., Chung, K., Teodosiu, C., 2009. Parameter identification of advanced plastic strain rate potentials and impact on plastic anisotropy prediction. Int. J. Plast. 25 (3), 491–512.

Roters, F., Eisenlohr, P., Hantcherli, L., Tjahjanto, D., Bieler, T., Raabe, D., 2010. Overview of constitutive laws, kinematics, homogenization and multiscale methods in crystal plasticity finite-element modeling: theory, experiments, applications. Acta Mater. 58 (4), 1152–1211.
Roters, F., Eisenlohr, P., Kords, C., Tjahjanto, D., Diehl, M., Raabe, D., 2012. DAMASK: the Düsseldorf advanced material simulation kit for studying crystal plasticity using an FE based or a spectral numerical solver. Procedia IUTAM 3, 3–10.
Rouet-Leduc, B., Barros, K., Cieren, E., Elango, V., Junghans, C., Lookman, T., Mohd-Yusof, J., Pavel, R.S., Rivera, A.Y., Roehm, D., McPherson, A.L., Germann, T.C., 2014. Spatial adaptive sampling in multiscale simulation. Comput. Phys. Commun. 185 (7), 1857–1864.
Rousselier, G., Barlat, F., Yoon, J., 2009. A novel approach for anisotropic hardening modeling. Part i: theory and its application to finite element analysis of deep drawing. Int. J. Plast. 25 (12), 2383–2409.
Saai, A., Dumoulin, S., Hopperstad, O., Lademo, O.-G., 2013. Simulation of yield surfaces for aluminium sheets with rolling and recrystallization textures. Comp. Mater. Sci. 67, 424–433.
Sachs, G., 1928. Zur ableitung einer filebedingung. Z. Des. Vereines Dtsch. Ingenieure 72, 734–736.
Savoie, J., MacEwen, S.R., 1996. A sixth order inverse potential function for incorporation of crystallographic texture into predictions of properties of aluminium sheet. Texture Microstruct. 26 (C), 495–512.
Segurado, J., Lebensohn, R.A., LLorca, J., Tomé, C.N., 2012. Multiscale modeling of plasticity based on embedding the viscoplastic self-consistent formulation in implicit finite elements. Int. J. Plast. 28 (1), 124–140.
Soare, S., Barlat, F., 2010. Convex polynomial yield functions. J. Mech. Phys. Solids 58 (11), 1804–1818.
Soare, S., Yoon, J.W., Cazacu, O., 2008. On the use of homogeneous polynomials to develop anisotropic yield functions with applications to sheet forming. Int. J. Plast. 24 (6), 915–944.
Taylor, G.I., 1938. Plastic strain in metals. J. Inst. Met. 62, 307–324.
Tjahjanto, D.D., Eisenlohr, P., Roters, F., 2010. A novel grain cluster-based homogenization scheme. Modell. Simul. Mater. Sci. Eng. 18 (1), 015006.
Tóth, L.S., Van Houtte, P., 1992. Discretization techniques for orientation distribution functions. Texture Microstruct. 19, 229–244.
Tsotsova, R., Böhlke, T., 2009. Representation of effective flow potentials for polycrystals based on texture data. Int. J. Mater. Form. 2 (S1), 451–454.
Van Bael, A., Eyckens, P., Gawad, J., Samaey, G., Roose, D., Van Houtte, P., 2010. Evolution of crystallographic texture and mechanical anisotropy during cup drawing. Steel Res. Int. 81, 1392–1395 (Supplement Metal Forming).
Van Houtte, P., 1988. A comprehensive mathematical formulation of an extended Taylor-Bishop-Hill model featuring relaxed constraints, the Renouard-Wintenberger theory and a strain rate sensitivity model. Texture Microstruct. 8–9 (C), 313–350.
Van Houtte, P., 1995. The MTM-FHM Software System Version 2.
Van Houtte, P., Delannay, L., Samajdar, I., 1999. Quantitative prediction of cold rolling textures in low-carbon steel by means of the Lamel model. Texture Microstruct. 31 (3), 109–149.
Van Houtte, P., Gawad, J., Eyckens, P., Van Bael, A., Samaey, G., Roose, D., 2011. A full-field strategy to take texture induced anisotropy into account during FE simulations of metal forming processes. JOM 63, 37–43.
Van Houtte, P., Li, S., Seefeldt, M., Delannay, L., 2005. Deformation texture prediction: from the Taylor model to the advanced Lamel model. Int. J. Plast. 21 (3), 589–624.
Van Houtte, P., Van Bael, A., 2004. Convex plastic potentials of fourth and sixth rank for anisotropic materials. Int. J. Plast. 20 (8–9), 1505–1524.
Van Houtte, P., Yerra, S.K., Van Bael, A., 2009. The facet method: a hierarchical multilevel modelling scheme for anisotropic convex plastic potentials. Int. J. Plast. 25 (2), 332–360.
Vegter, H., ten Horn, C.H.L.J., An, Y., Atzema, E.H., Pijlman, H.H., van den Boogaard, T.H., Huétink, H., 2003. Characterisation and modelling of the plastic material behaviour and its application in sheet metal forming simulation. In: Oate, E., Owen, D. (Eds.), Proceedings of COMPLAS VII. CIMNE, Barcelona (on CD–ROM).
Vegter, H., van den Boogaard, A., 2006. A plane stress yield function for anisotropic sheet material by interpolation of biaxial stress states. Int. J. Plast. 22 (3), 557–580.
Yin, Q., Zillmann, B., Suttner, S., Gerstein, G., Biasutti, M., Tekkaya, A.E., Wagner, M.F.-X., Merklein, M., Schaper, M., Halle, T., Brosius, A., 2014. An experimental and numerical investigation of different shear test configurations for sheet metal characterization. Int. J. Solids Struct. 51 (5), 1066–1074.
Yoon, J., Barlat, F., Dick, R., Karabin, M., 2006. Prediction of six or eight ears in a drawn cup based on a new anisotropic yield function. Int. J. Plast. 22 (1), 174–193.
Yoon, J.-H., Cazacu, O., Yoon, J.W., Dick, R.E., 2010. Earing predictions for strongly textured aluminum sheets. Int. J. Mech. Sci. 52 (12), 1563–1578.
Yoon, J.-W., Barlat, F., Dick, R.E., Chung, K., Kang, T.J., 2004. Plane stress yield function for aluminum alloy sheets–part ii: FE formulation and its implementation. Int. J. Plast. 20 (3), 495–522.
Yoon, J.W.J., Lou, Y., Yoon, J.W.J., Glazoff, M.V., 2014. Asymmetric yield function based on the stress invariants for pressure sensitive metals. Int. J. Plast. 56, 184–202.
Yoshida, F., Hamasaki, H., Uemori, T., 2013. A user-friendly 3D yield function to describe anisotropy of steel sheets. Int. J. Plast. 45, 119–139.
Zhang, K., Holmedal, B., Hopperstad, O.S., Dumoulin, S., Gawad, J., Van Bael, A., Van Houtte, P., 2015. Multi-level modelling of mechanical anisotropy of commercial pure aluminium plate: crystal plasticity models, advanced yield functions and parameter identification. Int. J. Plast. 66, 3–30.